The influence of lithospheric rheology and surface processes on the preservation of escarpments at rifted margins

João Pedro Macedo Silva [*], Victor Sacek, Rafael Monteiro da Silva

Instituto de Astronomia, Geofísica e Ciências Atmosféricas, Universidade de São Paulo, Rua do Matão, 1226, Butantã, São Paulo 05508-090, São Paulo, Brazil

ARTICLE INFO

ABSTRACT

The formation of rift flank topography along rifted margins is related to the flexural uplift of the footwall on the rift border fault during lithospheric stretching. The preservation of rift flank topography in mature margins can be explained as a feedback mechanism between differential denudation of the margin and regional isostatic response of the lithosphere. However, the contribution of the lithospheric rifting on the escarpment amplitude in both young and mature margins is not easily quantified. In the present work, we used a 2D thermo-mechanical numerical model to simulate lithospheric extension to evaluate the sensitivity of escarpment amplitude and its preservation under different rheological conditions over timescales larger than 100 Myr, comparable with the age of mature rifted margins. We found that the evolution of escarpment uplift and its preservation for tens of millions of years are sensitive to the degree of coupling between the crust and mantle and the regional isostatic response of the lithosphere to surface processes. The flexural uplift as a response to lithospheric stretching are limited to the first 100-150 km from the rift flank. Without the influence of surface processes, the amplitude of the escarpment monotonically decreases through time due to the lateral flow of the lower crust and thermal cooling of the margin. In the scenarios with surface processes, topographic signature inherited from the rift phase in the post-rift escarpment elevation is possible only in margins where the erosive escarpment retreat is smaller than ~100 km. In scenarios where the escarpment retreat exceeds this distance, the escarpment elevation is mainly preserved by the combination of the inherited topography (existent before the onset of lithospheric rifting) and flexural rebound of the lithosphere due to the erosion along the margin.

1. Introduction

Rifted margins represent a large portion of coastal margins worldwide [Bradley, 2008)] and several of these margins exhibit escarpments with more than one kilometer in amplitude, separating the continental interior from the coastal plain, either in young (e.g. Red Sea margins) or mature margins (e.g. Southeastern Australia, Western Ghats in India, and Brazilian and conjugate African margins along the South Atlantic margins) older than 80 Ma (Fig. 1). The topographic asymmetry between the steep coastal escarpment and the low relief continental interior has a profound impact on the denudation history along these margins. The higher slopes along the coastal escarpment contribute to facilitate the erosion by fluvial and hillslope processes, resulting in higher denudation rates along the margin relative to the continental interior [e.g. Sordi et al., 2018]. In fact, thermochronological data [e.g. Gunnell, 2000; van der Beek et al., 1995] show that apatite fission-track (AFT) ages along the coast are usually younger than the rifting age,

contrasting with AFT ages much older in the continental interior, indicating that a few kilometers of rock was eroded along the coastal plain since continental rifting [Braun et al., 2006]. The formation of steep escarpments along divergent margins indicate a clear relationship with the rifting process. For example, based on a global compilation of 40 margin escarpments with different ages and erosional histories, Osmundsen and Redfield [2011] showed that crustal thinning pattern and margin width has a inverse correlation with the height of the coastal escarpment.

To explain the formation of these escarpments along rifted margins and their preservation during the post-rift phase, different models were proposed during the last four decades based on analytical and numerical approaches [e.g. Beucher and Huismans, 2020; Braun, 2018; Braun and Beaumont, 1989; Burov and Poliakov, 2001; Gilchrist et al., 1994; Gilchrist and Summerfield, 1990; Kooi and Beaumont, 1994; van der Beek et al., 2002]. In regards to the mechanism of escarpment formation, the lithospheric stretching during continental rifting induces flexural

---

stresses that are regionally compensated by the lithosphere [Braun and Beaumont, 1989; Weissel and Karner, 1989]. As a consequence, the mechanical unloading of the lithosphere induces the formation of uplifted flanks at the borders of the rift by faulting. Additionally, other geodynamic processes were proposed in the literature that can amplify the elevation of escarpments along rifted margins during the rifting phase: (1) thermal effects due to the thinning of the lithosphere [Beaumont et al., 1982] and consequent uplift of the lithosphere-asthenosphere boundary (LAB); (2) magmatic underplating onto the continental crust [McKenzie, 1984; White and McKenzie, 1989], thereby increasing the effective thickness of the continental crust; and (3) dynamically supported by the impingement of mantle plumes [Turcotte and Emerman, 1983]. Among these processes, flexure and magmatic underplating can explain permanent uplift of the margin, while thermal effects due to lithospheric thinning are transient and hardly can contribute to preserve high altitudes in mature margins older than 60 Ma [Weissel and Karner, 1989]. However, the presence and geographic extension of magmatic underplating in onshore portions of mature rifted
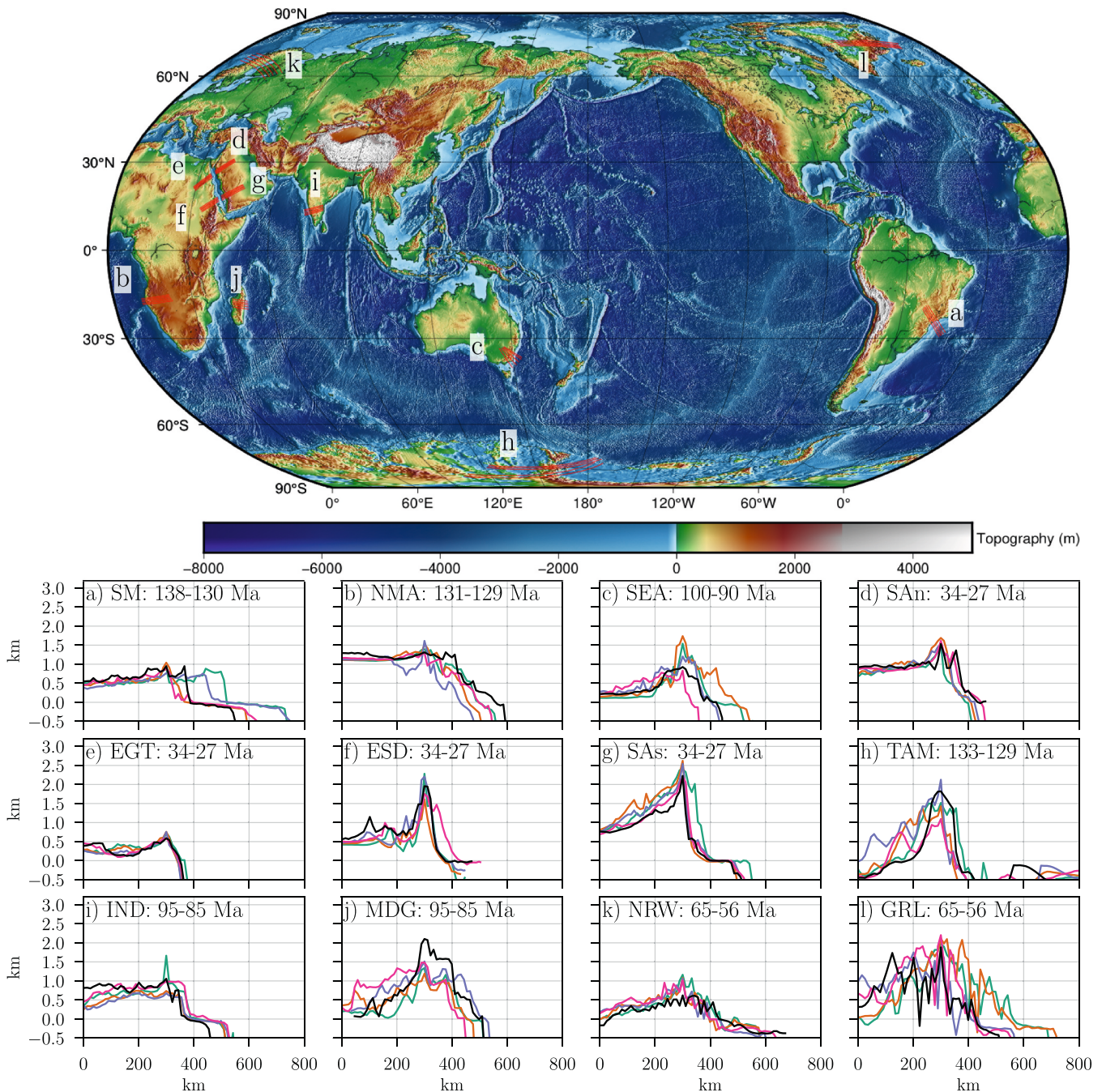
Fig. 1. Topographic map showing a selection of escarpments along rifted margins. Topography based on ETOPO1 [Amante and Eakins, 2009]. Red lines represents the oceanward topographic profiles crossing the coastal escarpments at rifted margins worldwide. (a-l): Topographic profiles described above. To improve visualization of the coastal escarpments of each margin, the profiles were aligned with the respective topographic maximum at $x = 300$ km. The time intervals indicate the rifting phase along each continental margin. SM: Serra do Mar; NMA: Namibia-Angola; SEA: Southeastern Australia; SAn: Northern Saudi Arabian; EGT: Egypt; ESD: Eritrea-Sudan; SAs: Southern Saudi Arabian; TAM: Transantarctic Mountains; IND: India (Western Ghats); MDG: Madagascar; NRW: Norway; GRL: Greenland. (For interpretation of the references to colour in this figure legend, the reader is referred to the web version of this article.)

margins is not clear [e.g. An and Assumpção, 2006], and seismic P-wave velocity structures in modern rifts indicate that underplating occurred essentially under the region of crustal thinning [Thybo and Artemieva, 2013]. The interaction of mantle convection with the base of the lithosphere can promote transient vertical perturbations of the lithosphere, known as dynamic topography, with amplitude of a few hundreds of meters and wavelength of hundreds to thousands of kilometers [Braun, 2010], which can amplify or reduce the elevation of the entire continental margin. Due to its transient behavior and relatively low amplitude, dynamic topography can just modulate the elevation of escarpments through the geological timescale.

The long-term preservation of the escarpment can be explained by the feedback between asymmetric erosion of the escarpment (mainly concentrated along the coast, with low erosion rates in the continental interior) and the flexural response of the lithosphere to the unloading of the margin [e.g. Gilchrist and Summerfield, 1990; Kooi and Beaumont, 1994], resulting in the partial rejuvenation of topography originally uplifted during rifting phase [see Braun, 2018, for a review]. For example, numerical simulations of surface processes and flexural isostasy in landscape evolution models [e.g. van der Beek et al., 2002] were successful in explaining the preservation of escarpments in mature margins and the exhumation history predicted by thermochronological data [e.g. Brown et al., 2002].

During the last decades, the formation of the coastal escarpment during lithospheric stretching and the long term preservation of the escarpment were explored independently in the literature. Notable exceptions are works that integrated thermo-mechanical models and landscape evolution models mainly during the rifting phase [e.g. Burov and Poliakov, 2001]. Only a few papers explored the long-term evolution of escarpments after the onset of lithospheric rifting, extending the analysis to post-rift phase: Theunissen and Huismans [2019] simulated the formation and evolution of divergent margins for a time span of 40 Myr, concluding that surface processes of erosion and sedimentation contribute to enhance strain localization and control margins architecture and that the post-rift regional isostatic response to unloading stabilizes the water drainage divide initially formed by the rift flank and controls its migration speed. Beucher and Huismans [2020] observed that ductile flow of the lower crust affects the amplitude of the escarpment in thermo-mechanical simulations spanning 10 Myr and Wolf et al. [2022] simulated the evolution of divergent margins for a time interval of 40 Myr, showing how the increase in erosion and sedimentation rate along the margin contribute to induce strain localization during lithospheric rifting and confirmed that post-rift capture of the hinterland drainage network is responsible for transient high sediment flux.

In the present work we explored the formation and evolution of coastal escarpments along rifted margins while considering a time interval larger than 100 Myr, compatible with the longevity of the conjugate margins between Brazil and Africa, for example. We aim to quantify the contribution of rift flank topography on the present day morphology of great escarpment by using 2D thermo-mechanical numerical models to simulate lithospheric stretching and to analyse the preservation of the obtained escarpment related to different magnitudes of erosional retreat.

2. Model description

To simulate the formation and evolution of rifted margins, we used the finite element code called Mandyoc [Sacek, 2017; Silva and Sacek, 2022] that numerically solves the Stokes's flow equations for an incompressible non-Newtonian fluid resulting in the following differential equations of conservation of mass, energy and momentum, respectively [Zhong et al., 2007]:

$$u_{i,i} = 0 \qquad (1)$$

$$\sigma_{ij,j} + g_i \rho = 0 \qquad (2)$$

$$\frac{\partial T}{\partial t} + u_i T_{,i} = \kappa T_{,ii} + \frac{H}{c_p} + u_i g_i \alpha \frac{T}{c_p} \qquad (3)$$

where

$$\sigma_{ij} = -P\delta_{ij} + \eta(u_{i,j} + u_{j,i}), \qquad (4)$$

$$\rho = \rho_0[1 - \alpha(T - T_0)], \qquad (5)$$

and t is time, u_i is the i-th velocity component, g is gravity, ρ_0 is the reference rock density at temperature $T_0 = 0\ °C$, α is the coefficient of thermal expansion, T is temperature, κ is the thermal diffusivity, H is heat production per unit of mass, c_p is specific heat capacity, P is the total pressure, η is the dynamic viscosity and δ_{ij} is the Kronecker delta. Repeated indices mean summation and the indices after commas represent the partial derivative to the respective coordinate.

We adopted a visco-plastic rheology to represent the geodynamic evolution of the crust and mantle, where the effective viscosity η combines the non-linear power law viscous rheology and a plastic yield criterion. The viscous component is a function of temperature and composition [Huismans and Beaumont, 2014]:

$$\eta_{\text{visc}} = CA^{-1/n}\dot{\varepsilon}_{II}^{\frac{1-n}{n}} exp\left[\frac{E_a + VP}{nRT}\right] \qquad (6)$$

where C is a scale factor, A is the pre-exponential scale factor, n is the power law exponent, $\dot{\varepsilon}_{II}$ is the square root of the second invariant of deviatoric strain rate tensor given by $\left(\frac{1}{2}\dot{\varepsilon}'_{ij}\dot{\varepsilon}'_{ij}\right)^{1/2}$, E_a is the activation energy, V is the activation volume, and R is the universal gas constant.

In the plastic regime, brittle failure occurs when the stress in the rock reaches the Drucker-Prager criterion, which is equivalent to Mohr-Coulomb criterion under plane strain conditions [Wojciechowski, 2018]:

$$\sigma_{yield} = c_0 cos\phi + P sin\phi, \qquad (7)$$

where ϕ is the internal angle of friction and c_0 is the internal cohesion of the rock and both vary linearly as a function of cumulative strain ε during strain softening which facilitates the localized deformation [Huismans and Beaumont, 2003]. Below and above the limits of strain softening presented in Table 1, c_0 and ϕ are assumed constant.

The combination of the plastic and viscous components result in the effective nonlinear viscosity, given by [Moresi and Solomatov, 1998]:

$$\eta = min(\eta_{\text{plast}}, \eta_{\text{visc}}) = min\left(\frac{\sigma_{yield}}{2\dot{\varepsilon}_{II}}, \eta_{\text{visc}}\right). \qquad (8)$$

The topographic response due to extension is simulated by the sticky-air approach [Crameri et al., 2012] where a layer of low density and low viscosity is inserted above the upper crust to emulate the air and the topographic response is obtained by mapping the interface between air layer and upper crust.

The composition and the cumulative strain are tracked through time by particles that permeate each finite element of the domain. Initially, each element contains nearly 160 particles uniformly distributed.

2.1. Model setup

The model domain (Fig. 2a) has $1600 \times 300\ km^2$ with 2 km of grid resolution in both directions, resulting in 120000 finite elements. The domain is subdivided into five layers: air, upper crust, lower crust, lithospheric mantle, and asthenospheric mantle. The thickness of each layer is, respectively, 40, 20, 15, 95 and 130 km resulting in a lithosphere with 130 km thick. Inside the lithospheric mantle there is a 6×6 km^2 weak seed of same composition but with lower cohesion and internal friction angle, representing a local heterogeneity that helps the

Table 1

Rheological parameters of numerical scenarios according to respective layer.

Description	Symbol	Unit	Air	Upper Crust	Lower Crust	Lithospheric Mantle	Asthenosphere
Creep flow law	–	–	–	Wet quartz[1]	Wet quartz[1]	Dry olivine[2]	Wet olivine[2]
Power law expoent	n	–	1	4	4	3.5	3
Scale Factor	C	–	1	1	1, 2, 5, 10, 40	1	1
Reference density	ρ_0	kg/m^3	1	2700	2800	3354	3378
Pre-exponent constant	A	Pa^{-n}/s	1.0×10^{-18}	8.574×10^{-28}	8.574×10^{-10}	2.4168×10^{-15}	1.393×10^{-14}
Activation Energy	E_a	kJ/mol	0	222	222	540	429
Activation Volume	V	m^3/mol	0	0	0	25×10^{-6}	15×10^{-6}
Heat Production[3]	H	W/kg	0	9.26×10^{-10}	2.86×10^{-10}	9.0×10^{-12}	0
Cohesion[4]	c_0	MPa	–	20→4	20→4	20→4	20→4
Internal friction angle[4]	$\phi_{eff}(\varepsilon)$	–	–	15°→2°	15°→2°	15°→2°	15°→2°
Strain softening interval[4]	–	–	–	1.05→0.05	1.05→0.05	1.05→0.05	1.05→0.05

[1] Extracted Gleason and Tullis [1995].
[2] Extracted from Karato [1993].
[3] Extracted from Andrés-Martínez et al. [2019] for upper and lower crust.
[4] Extracted from Salazar-Mora et al. [2018]
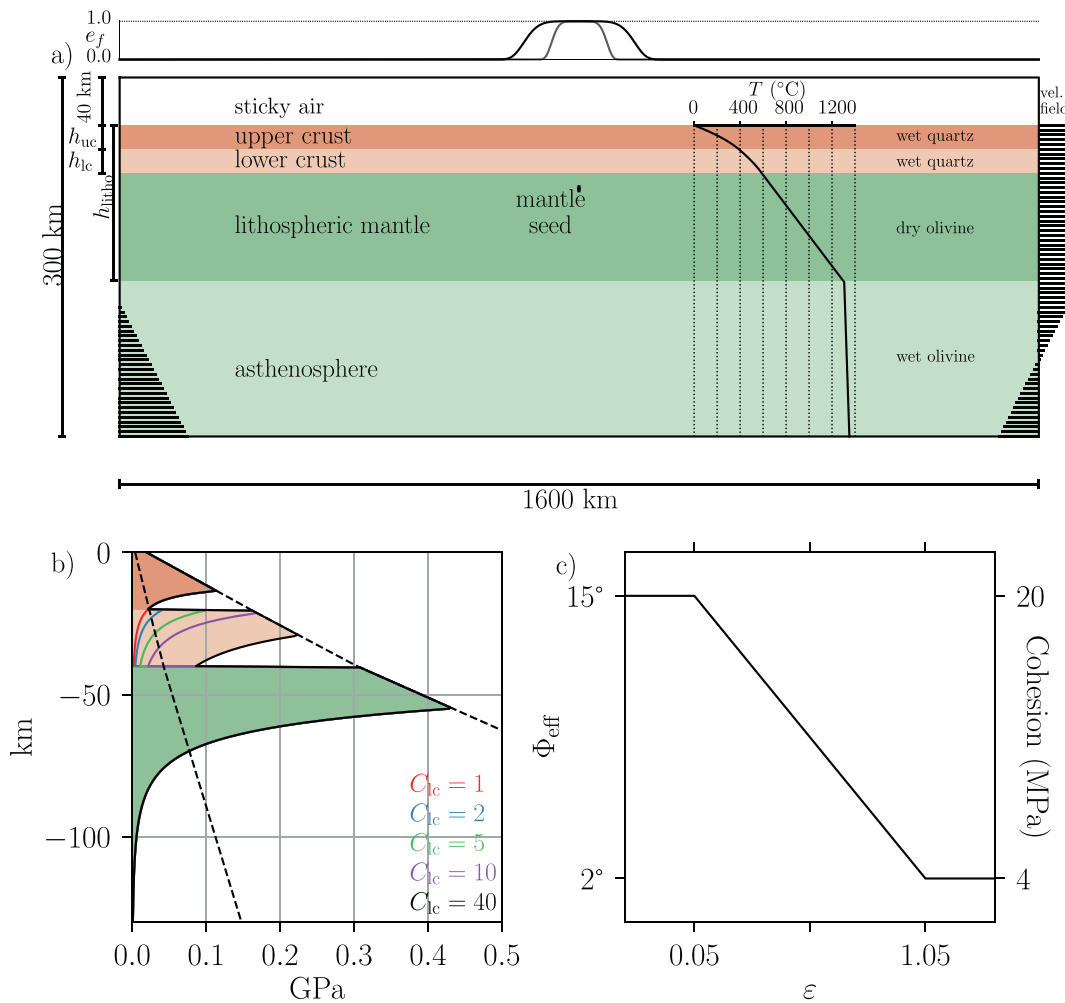
Fig. 2. a) Initial numerical setup for the experiments. $h_{uc} = 20$ km, $h_{uc} = 15$ km and $h_{litho} = 130$ km are the thickness of upper crust, lower crust and lithosphere, respectively (see text for details about layers and boundary conditions). Gray and black curves represent the region where surface processes acts for scenarios with $x_\sigma = 50$ and 100 km, respectively. b) Initial yield strength envelopes (YSE) for numerical scenarios according to the scale factor adopted for the lower crust, C_{lc} (Eq. 6 and text for more details), represented by the different colors: red: $C_{lc} = 1$; blue: $C_{lc} = 2$; green: $C_{lc} = 5$; purple: $C_{lc} = 10$; black: $C_{lc} = 40$. The curves were drawn assuming $\dot{\varepsilon}_{II} = 10^{-5}$ s^{-1}. Dashed lines represent the plastic strain yield criterion for the maximum and minimum internal angle of friction ϕ and internal cohesion c_0 adopted. c) Strain softening. (For interpretation of the references to colour in this figure legend, the reader is referred to the web version of this article.)

nucleation of rifting in the center of the model domain [Huismans and Beaumont, 2007; Huismans and Beaumont, 2003]. Free surface is simulated by the "sticky air" approach, as described above (Fig. 2a, Table 1).

The initial thermal structure of the lithosphere is only depth dependent and is represented by the black vertical profile inside the inset plot in Fig. 2a. This profile is obtained by the solution of the steady state diffusion equation with the source term:

$$\kappa\frac{\partial^2 T(z)}{\partial z^2} + \frac{H(z)}{c_p} = 0, \tag{9}$$

where $H(z)$ is the internal heat production of each layer (Table 1) assuming that the surface is at 0 °C and the base of the lithosphere is at 1300 °C. The sub-lithospheric temperature increases adiabatically up to the bottom of the domain:

$$T = T_p exp\big(g\alpha z/c_p\big), \tag{10}$$

where T_p= 1262 °C is the potential temperature for the mantle. Additionally, the temperature in all boundaries was fixed during the numerical simulations and the nodes in the air layer was maintained at 0 °C.

The velocity boundary conditions are represented by the horizontal black lines at the vertical borders in Fig. 2a and were chosen to ensure the conservation of mass following the same procedure adopted by Silva and Sacek [2022]. In this procedure new material enters the asthenospheric mantle on the sides to compensate the removed material at the right border by the lithospheric stretching. The reference frame is fixed on the left portion of the model and the lithosphere on the right moves rightward with a constant velocity.

In our numerical scenarios, we assumed a simplified approach to simulate the denudation of the margin, adopting a prescribed denudation rate and predefined extent of the escarpment retreat, which facilitates the comparison of the different thermomechanical scenarios with different rheological structures but similar denudation history. The erosion of the coastal escarpment is simulated by the expression presented in Silva and Sacek [2022]:

$$\dot{e}(x) = k_{sp}e_f(x) \quad for \ t > 10 \ Myr, \tag{11}$$

where, k_{sp} is the maximum denudation rate and e_f is the spatial control of denudation, given by:

$$e_f(x) = exp\left[-\frac{(x - x_c)^6}{x_\sigma^6} \right]. \tag{12}$$

x_σ controls the spatial extent of denudation from the center of the model at position $x = x_c$, and t is time since the onset of the numerical simulation. Erosion acts only if the topographic surface is above sea level ($h > h_{sl}$). The parameters used in the surface processes are presented in Table 2. Additionally, for $e_f < 1.0 \times 10^{-5}$ the denudation rate is imposed to be null. This condition is used here to control the maximum escarpment retreat to be of the same order of x_σ. Therefore, with this approach, we can know the magnitude of escarpment retreat a priori.

In each time step for the surface processes model, the land/air interface is tracked by the limit between the "sticky air" and crust particles. After the application of the erosion on this interface, the new free surface is calculated and all crustal particles above this interface are transformed to "sticky air" particles.

Other previous numerical models explored more realistic surface processes formulations, as the stream power law to describe the fluvial dynamics [e.g. Theunissen and Huismans, 2019], where the surface processes are influenced by the internal dynamics that continuously perturbs the landscape. In our simplified approach, the prescribed

Table 2
Fixed thermal and erosional parameters.

Description	Symbol	Value	Unit
Volumetric expansion coefficient	α	3.28×10^{-5}	K^{-1}
Thermal diffusivity	κ	10^{-6}	m^2/s
Specific heat capacity	c_p	1250	J/kg/K
Half-width for the denudation function	x_σ	50,100	km
Position of maximum denudation	x_c	800	km
Maximum denudation rate	k_{sp}	4×10^{-3}	m/yr
Sea level relative to the initial altitude	h_{sl}	-1000	m

denudation curve controls the maximum retreat of the coastal escarpment only, facilitating the classification of the scenarios in terms of magnitude of escarpment retreat. We do not consider sedimentation, because the sedimentation during the rifting process can induce thermal effects that changes lithospheric rheology and the margin geometry as well [Buiter, 2021].

2.2. Classification of numerical scenarios

The scenarios are classified into three main groups according to the action of surface processes during simulation: Group I, scenarios without erosion, and groups II and III with erosion.

The denudation in the scenarios of groups II and III assumed $x_\sigma = 50$ km and 100 km, respectively (Fig. 2a). Therefore, the escarpment retreat in the scenarios of Group II is nearly 50 km and in the scenarios of Group III is nearly 100 km. The exact value of escarpment retreat varies between the simulations, depending on the initial position of the escarpment.

To evaluate the impact of stretching rate on the escarpment formation and evolution, we subdivided Group I into three subgroups, I-a, I-b, and I-c, with different velocities for the lithospheric stretching, 1, 0.5 and 0.25 cm/year, respectively.

For each group and subgroup, different values for viscosity scale factor C (Eq. 6) were assumed for the lower crust, C_{lc}: 1, 2, 5, 10 and 40 (see Fig. 2b). These values represent the degree of coupling between the crust and lithospheric mantle. For example, a lower crust with $C_{lc} = 40$ is 40 times more viscous at the same temperature, pressure and strain rate conditions compared to $C_{lc} = 1$. Hence, large values of C_{lc} represent a stronger crust-mantle coupling.

For the groups II and III, the denudation processes starts at 10 Myr after the onset of lithospheric stretching. This delay is intended to ensure that the stretching history of groups I, II, and III for the same C_{lc} are the same during the first 10 Myr of lithospheric stretching, resulting in margins with similar geometry, facilitating the comparison between the simulations with the same rheological structure but different denudation history.

3. Results

First, we describe the results from the numerical scenarios of subgroups I-a I-b and I-c, which does not include surface processes, evaluating the impact of lithospheric rheology variation and extension rate on the margin architecture and amplitude of the escarpments. Then, we compare the Group I-a results with groups II and III, which incorporates surface processes and different amount of escarpment retreat.

3.1. The influence of crust-mantle coupling degree on margin architecture and escarpment formation

Based on the scenarios of subgroup I-a, I-b and I-c, the degree of crust-mantle coupling affected the strain pattern of the lithosphere (Fig. 3) and the final length of the margins (Fig. 4). The scenarios with $C_{lc} = 1$ and 2 presented wider margins with combined margins reaching at least 260 km in length (Fig. 4a-f). In these cases, stretching is mainly accommodated by ductile flow of the lower crust and the plastic deformation is concentrated primarily in the upper crust and parts of the lithospheric mantle (Fig. 3).

On the other hand, for scenarios with $C_{lc} = 5$, 10 and 40, the rifting is more localized and the width of the combined conjugate margins is <220 km (Fig. 4e-o). These scenarios contain a strong lower crust and the normal faulting during lithospheric stretching is focused in the central region of the rift. During the syn-rift phase, the strong lower crust hampers the lateral flow and facilitates the concentration of deformation at the center of rift (Fig. 3) producing a narrow margin with low amount of viscous deformation (Fig. 4).

Additionally, the scenarios with $C_{lc} = 1$ and 2 resulted in a protracted
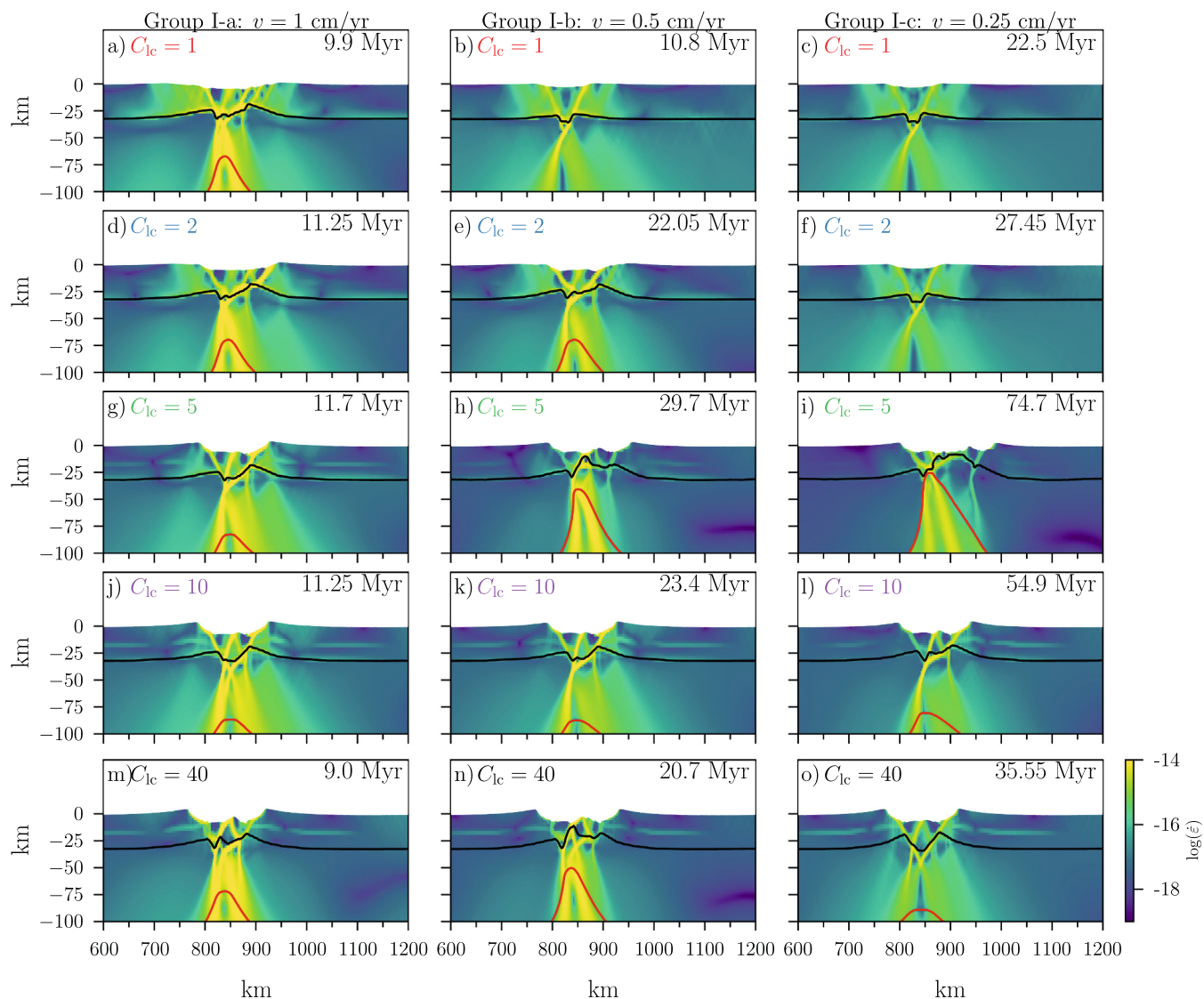
Fig. 3. Strain rate pattern at the instant of maximum amplitude of rift flank for scenarios of groups I-a (1st column), I-b (2nd column) and I-c (3rd column). Each row represents the adopted C_{lc} = 1 (a-c), 2 (d-f), 5 (g-i), 10 (j-l) and 40 (m-o), respectively. Black and red lines represent the base of the lower crust and lithospheric mantle, respectively. (For interpretation of the references to colour in this figure legend, the reader is referred to the web version of this article.)

flow of the lower crust in response to flexural and isostatic restoration of equilibrium (Fig. 4a-f), impacting the evolution of the margin. This post-rift flow of the lower crust is less expressive in the scenarios with relatively high viscosity for the lower crust.

The scenarios of reference group (I) produced coastal escarpments in both conjugate margins with amplitude sensitive to the rheological structure of the lithosphere. In the scenarios with a weak lower crust and consequent low degree of crust-mantle coupling, the distributed stretching resulted in coastal escarpments with low amplitude, with maximum uplift between 1 and ~3 km (Fig. 5a-f). However, in scenarios with a stronger crust-mantle coupling, the maximum uplift of the coastal escarpment can reach >4 km (Fig. 5g-o).

The wavelength of the flexural response that created the coastal escarpment is similar in all experiments of this group (≈100–150 km, see Fig. 5), creating a negative flexural bulge in the interior of the continent with an amplitude of a few hundreds of meters.

The escarpments along the conjugate margins are partly asymmetric and the degree of asymmetry depends mainly on the degree of coupling between crust and lithospheric mantle (Fig. 5). We can measure the evolution and the degree of symmetry between each escarpment by

tracking the top of rift flank (escarpment top) over time. At the end of *syn*-rifting phase (~ 17–20 Myr for Group I-a), the escarpment amplitude (the elevation difference between the plateau and the maximum elevation of the escarpment) decreases near monotonically due to dissipation of stresses in the lithosphere and thermal cooling of the margin (Fig. 6). In the first 25 Myr, margins with a strong lithospheric coupling are more symmetric than those with weak crust-mantle coupling. The greatest asymmetry were observed in scenarios with intermediate degree of crust-mantle coupling (C_{lc} = 2 and 5).

3.2. The influence of stretching rate on the margins evolution

In scenarios of subgroups I-a, I-b, and I-c, the timing for breakup and the combined margins lengths increased as the extension rate decreased (Fig. 4). Additionally, for scenarios with a lower crustal strength (Fig. 4a-f), the width of the conjugate margins become more asymmetric as the extension rate decreased. For example, for C_{lc} = 1, the margins formed with an extension velocity v = 1 cm/year have nearly symmetric widths (132 and 136 km, Fig. 4a). On the other hand, the same scenario with v = 0.25 cm/year created margins with larger asymmetry (152 and
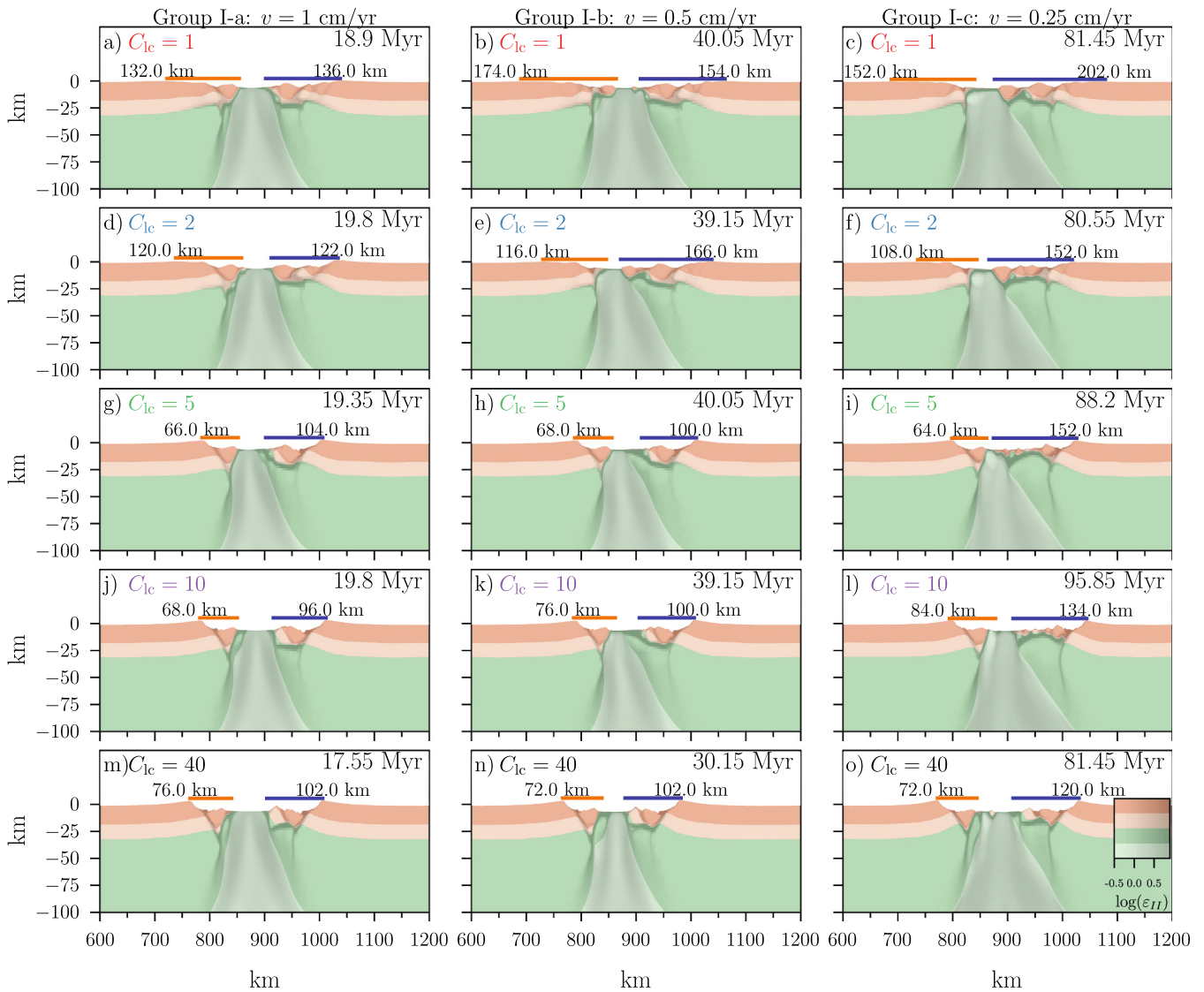
Fig. 4. Margin geometry right after the end of *syn*-rift phase (breakup) for scenarios of groups I-a (1st column), I-b (2nd column) and I-c (3rd column). Each row represents the adopted C_{lc} = 1 (a-c), 2 (d-f), 5 (g-i), 10 (j-l) and 40 (m-o), respectively. Shaded areas represents the cumulative strain. Dark and light orange represents upper and lower crust, respectively. Dark and light green represents lithospheric mantle and asthenosphere, respectively. Orange and blue horizontal bars indicates the width of left and right margins, respectively. The margin width is measured by the distance from the top of rift flank (escarpment) to the end of continental crust. (For interpretation of the references to colour in this figure legend, the reader is referred to the web version of this article.)

202 km). This effect is attenuated as the lithospheric strength increases and the margins become narrower (Fig. 4g-o). For some of the scenarios with slow extension (v = 0.25 cm/year), the wider margin becomes hyperextended, with extended crust thinner than 15 km, for a region wider than 100 km (see right margin for scenarios in Fig. 4i,l). Also note that continental lithospheric mantle necking is slower with decreasing spreading rate. The effect of strain localization due to thermal necking is therefore reduced resulting in more distributed deformation and wider margins.

When the stretching rate decreases, all the rifting processes become slower and, consequently, the timing for the instant of maximum amplitude of rift flanks occurs later (Fig. 3 and Fig. S2). For example, for C_{lc} = 2, the time interval between the onset of lithospheric stretching and the maximum amplitude of the marginal escarpment is ~11 Myr for v = 1 cm/year and ~27 Myr for v = 0.25 cm/year. However, the amplitude of the coastal escarpment is less sensitive to the stretching rate (compare the different columns in Fig. 5). Only for the scenarios with low degree of crust-mantle coupling, with C_{lc} = 1 and 2, the escarpment amplitude is lower for slower stretching rates (Fig. 5a-f).

3.3. Influence of erosion on the evolution of escarpment amplitude

The same numerical scenarios of Group I-a were simulated considering the influence of erosion (Fig. 7). For Group II, the escarpment retreat is nearly 50 km, while for the Group III, the escarpment retreat is nearly 100 km.

The scenarios in Group III represent margins where the erosion of the escarpment is very effective, with a retreating distance similar to the one observed along the continental margin of southeastern Brazil. In the Brazilian margin the distance between the Cretaceous hinge line and the present Serra do Mar escarpment is >100 km [Silva and Sacek, 2022]. In both Groups II and III the initial continental interior elevation is assumed to be 1 km above the sea level. As a comparison, the elevation of stable continental portions far from the influence of hotspots is 400 ±400 m [Theunissen et al., 2022]. Therefore, the initial value of 1000 m above the sea level adopted here represents an upper limit for stable continental regions far from the influence of hotspots. However, many divergent margins contain regional elevation above 1 km, like the Southern Africa margins (Fig. 1b) and Saudi Arabian margins (Fig. 1d,g).
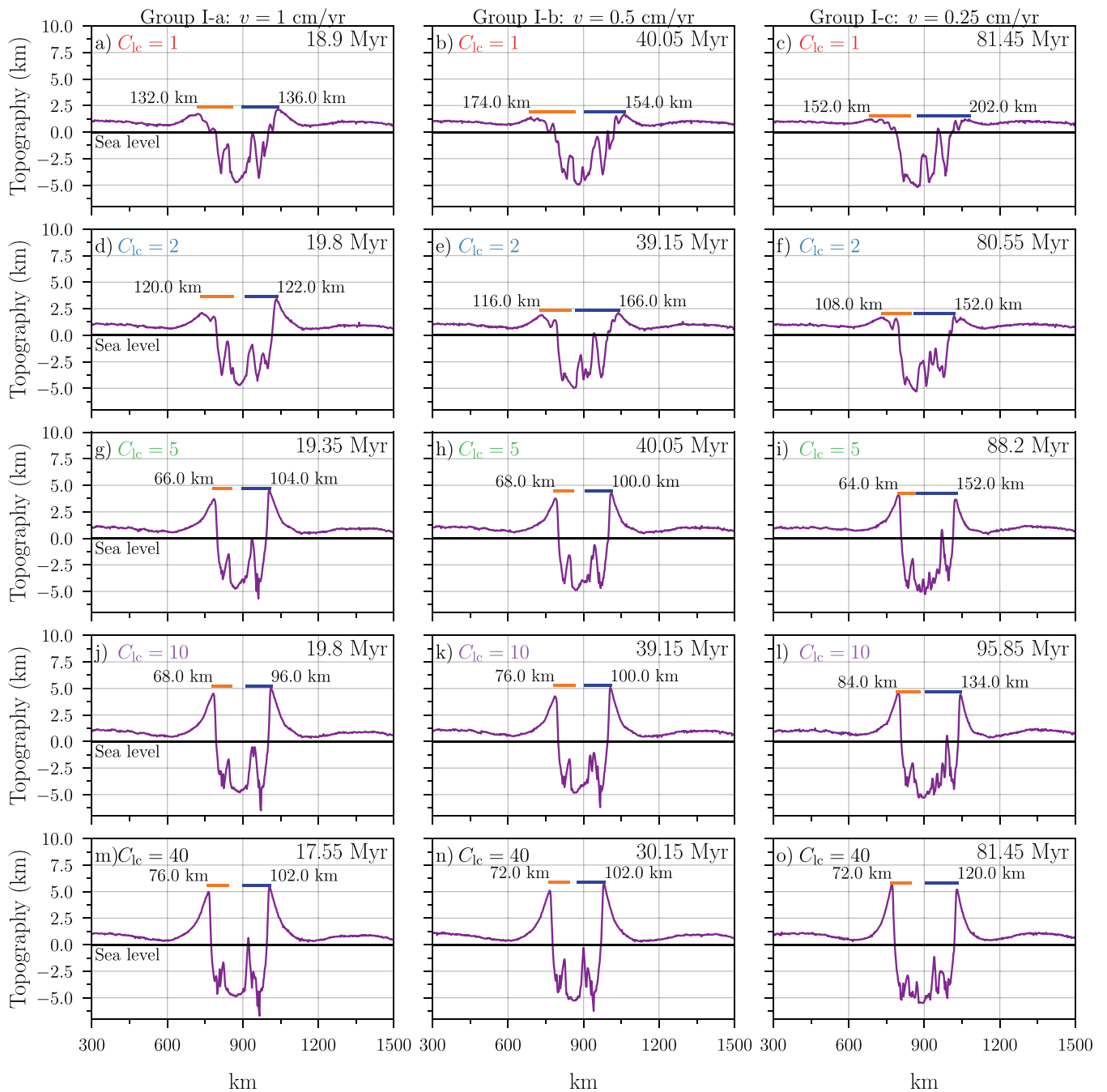
Fig. 5. Topography for scenarios of groups I-a (1st column), I-b (2nd column) and I-c (3rd column) right after the end of *syn*-rift phase (breakup). Each row represents the adopted $C_{lc} = 1$ (a-c), 2 (d-f), 5 (g-i), 10 (j-l) and 40 (m-o), respectively. The initial elevation is 1 km above sea level. Orange and blue horizontal bars indicates the width of left and right margins, respectively. Level. (For interpretation of the references to colour in this figure legend, the reader is referred to the web version of this article.)

In Fig. 8 we present the topographic evolution of the left margin for groups I-a, II and III. After 130 Myr of numerical simulation, the scenarios of Group I-a (Fig. 8 first column) have escarpments with amplitudes that are related to the degree of coupling between crust and lithospheric mantle, with the strong coupled scenarios producing well-developed escarpments at the end of simulation (Fig. 8c-e).

In scenarios with intermediate retreat (Group II, Fig. 8 second column), the final position of the escarpment is still under the flexural influence of the topography created by rift flank uplift of the border fault during the syn-rift phase (Fig. 7 for $x_\sigma = 50$ km). In the scenarios of Group III (Fig. 8 third column), the escarpment amplitude, at the final

position nearly 100 km far from the initial location, has no relation with the initial amplitude. In these cases, the amplitude of the escarpment is close to the height of the initial 1 km plateau (Fig. 7 for $x_\sigma = 100$ km).

An interesting effect observed during the long term simulation of the evolution of the margin is the evolution of the negative forebulge developed in the interior of the continent. This depression originated during the rifting phase, reaching a few hundreds of meters, is not geographically fixed through time, and its depocenter movies towards the escarpment for a distance of 40–80 km in the scenarios of Group I and II. On the other hand, in the scenarios of Group III the depocenter of the negative forebulge was nearly stationary. Additionally, the
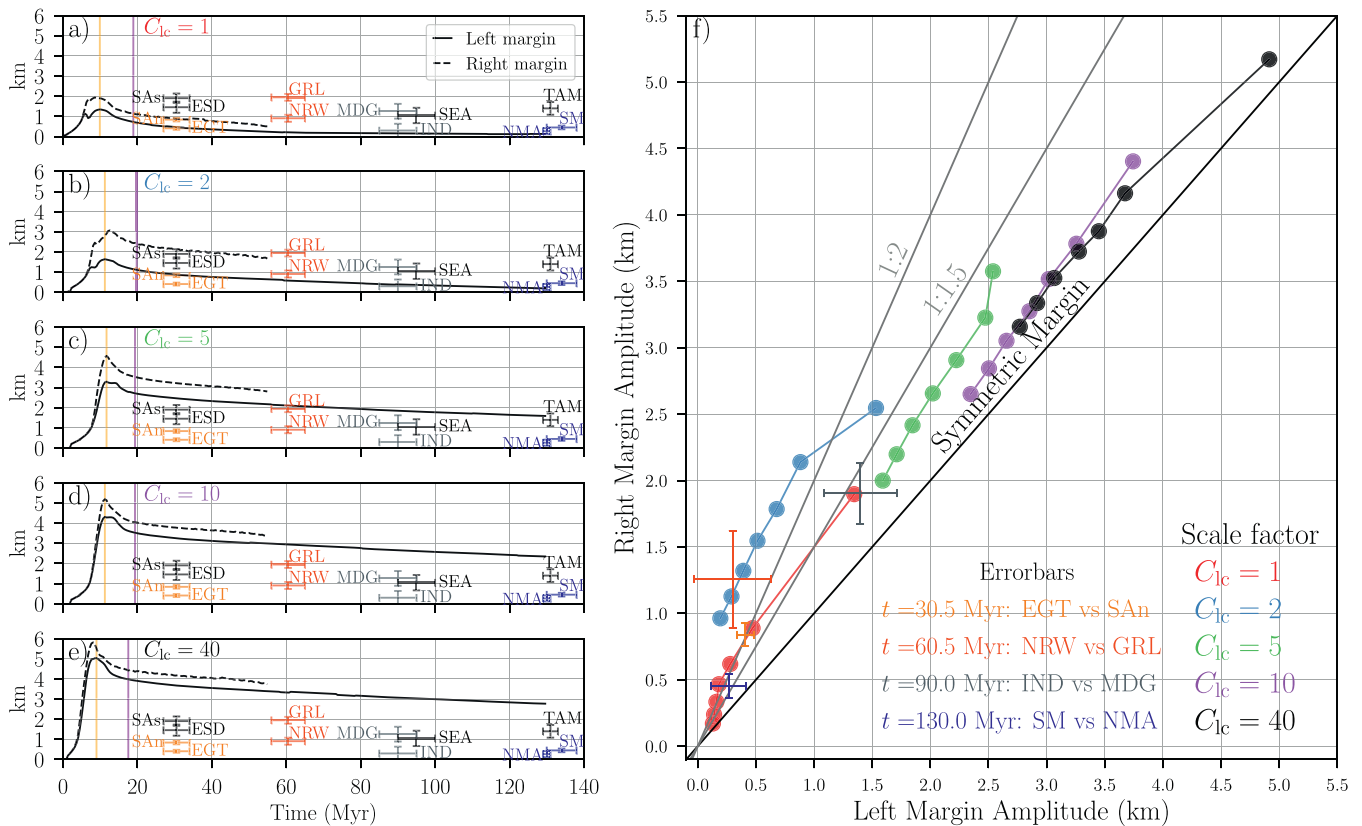
Fig. 6. (a-e) Evolution of the escarpment amplitude (elevation difference between maximum escarpment elevation and the plateau) of left (solid lines) and right (dashed lines) margins for scenarios of Group I-a. Error bars represent the mean amplitude of escarpments derived from the residual topography ($\bar{h}_{res}$) of the natural margins according to margin age as presented in Table S1. The amplitude of the right margin is plotted until 60 Myr, when this margin is out of the numerical domain. f) Evolution of symmetry of left and right escarpment for Group I-a from 10 to 130 Myr with a time step of 20 Myr. Escarpments for each subgroup are colour-coded for the scale factor C_{lc}: 1 (red), 2 (blue), 5 (green), 10 (purple) and 40 (black). For $t > 60$ Myr, we extrapolated the amplitude of the right margin escarpment through time (see Supplemental Material). Error bars represent the mean amplitude of escarpments of residual topography from natural margins. Black and gray lines represents the ratio of amplitude between margins. SM: Serra do Mar, NMA: Namibia-Angola; SAn: Northern Saudi Arabian; EGT: Egypt; IND: India (Western Ghats); MDG: Madagascar; NRW: Norway; GRL: Greenland.

magnitude of subsidence is attenuated in the scenarios with imposed erosion (see movies of the topographic evolution in the Supplementary Materials).

The amplitude of the escarpment decreased faster according to the amount of retreat for scenarios with strong lower crust (Fig. 9c-e). Curiously, for a weak crust ($C_{lc} = 1, 2$), the scenarios with intermediate retreat presented a better preservation of rift flank topography (Fig. 9a-b, green curves), probably as a result of the combined effect of rift flank uplift and regional uplift due to the limited erosional exhumation of the margin.

4. Discussion

4.1. The formation and long-term evolution of escarpments at rifted margins

From the numerical experiments presented in this work, we observed that the amplitude of the rift flank uplift is controlled by the flexural rigidity of the lithosphere: the scenarios with a higher degree of coupling between crust and mantle developed the highest escarpment along the conjugate margins. This pattern was previously reproduced and observed in other thermo-mechanical models for the evolution of rifted margins [e.g. Beucher and Huismans, 2020; Theunissen and Huismans, 2019], exploring the variation of the effective viscosity of the lower crust, the same procedure adopted here.

In the scenarios without surface processes, we observed that the

stretching rate affected the width and symmetry of the margins, also influencing the longevity of the rifting phase. However, the amplitude of the escarpments is not significantly affected by the stretching rate. Only the timing for the maximum escarpment uplift is delayed when the stretching rate is slow as in the models of Wolf et al. [2022].

In our simulations of >100 Myr without surface processes, we observed that the amplitude of the coastal escarpment decreases through time independent of the degree of coupling between crust and lithospheric mantle. This occurs due to the combined effect of thermal cooling of the margin during the post-rift phase and viscous dissipation, mainly in the lower crust. After 130 Myr, the scenarios with a high degree of coupling ($C_{lc} \geq 5$) and no erosion preserved more 1.5–2.9 km of topographic uplift. On the other hand, the scenarios with $C_{lc} \leq 2$ and no erosion preserved <0.3 km of escarpment uplift. For the scenarios with escarpment retreat due to surface processes, the decrease in escarpment amplitude is mainly guided by erosion, and the height of the escarpment tends to be of the same order of the pre-rift topography of the continental interior which is prescribed by the sea level.

Adjacent to the rift flank uplift, the negative forebulge also evolves through time, both in amplitude and geographic position. During the post-rift phase of the margin, thermal cooling of the margin induces the regional subsidence of the escarpment and part of the continental interior. Without erosion, this effect induces the tilt of the continental interior and displaces the depocenter of the negative forebulge for 40–80 km towards the coast. This negative forebulge has an important impact on the drainage pattern in the continental interior, controlling
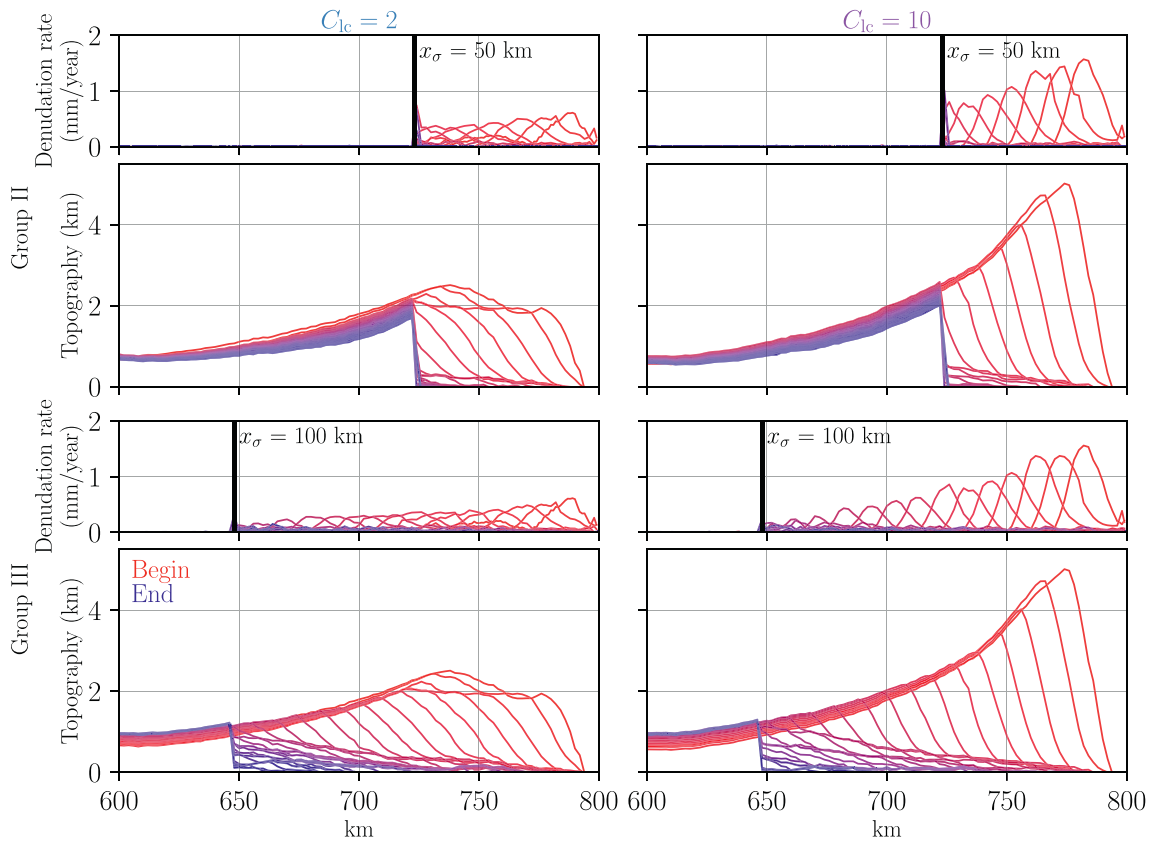
Fig. 7. Denudation rate and topographic evolution of the coastal escarpment on the left margin for four scenarios: with $C_{lc} = 2$ (left column) and 10 (right column) and half-width for the denudation function for $x_\sigma = 50$ (Group II) and 100 km (Group III). The vertical black line indicates the maximum escarpment retreat in each scenario. The curves from red to blue represent the elevation of the escarpment and the mean denudation rate in intervals of nearly 2.2 Myr, starting at 10 Myr from the onset of the numerical simulation. (For interpretation of the references to colour in this figure legend, the reader is referred to the web version of this article.)

the development of axial rivers parallel to the coast [Jiao et al., 2020; Sacek et al., 2012]. Based on our results, when the magnitude of the erosion of the coastal escarpment is small, the thermal subsidence of the margin can contribute to displace the axial river a few tens of kilometers towards the coast. However, when the escarpment retreat is of the order of 50–100 km, this induces an upward flexural response of the margin, compensating the thermal subsidence of the margin. In this case, the axial river along the depocenter of the negative forebulge is preserved almost at the same location, with attenuated amplitude.

4.2. Preservation of escarpments in mature margins

Coastal escarpments worldwide have unique evolution histories, being impacted by different geological events, including regional uplift due to mantle dynamics and erosive events caused by climate changes [Burov and Cloetingh, 1997; Chery et al., 1992; Nyblade and Sleep, 2003; Ryberg et al., 2015; van der Beek et al., 1995; Widdowson and Cox, 1996]. We can express the elevation of the present margin escarpment h as the summation of (1) the preexistent (pre-rift) topography h_0 before the onset of the rifting phase, (2) the vertical movements of the surface induced by fault slip during lithospheric stretching and consequent thermal effects (Δh_{rift}), and (3) the post-rift events that are not directly related to the rifting processes but can modify the elevation of the margin (Δh_{post}):

$$h(x_r, t) = h_0(x_r) + \Delta h_{rift}(x_r, t) + \Delta h_{post}(x_r, t) \tag{13}$$

where x_r is the amount of escarpment retreat and t is the time interval since the onset of rifting.

The rifting component Δh_{rift} is related to the rift flank uplift of the

border fault during lithospheric stretching and consequent thermal perturbations due to the thinning of the lithosphere. These physical effects can be quantified in our thermo-mechanical scenarios of Group I-a (Fig. 6), where Δh_{rift} reaches a maximum value during the end of lithospheric rifting and decreases monotonically during the post-rifting phase.

In scenarios with low crust-mantle coupling ($C_{lc}=1$, Fig. 6a), Δh_{rift} decreases mainly in the first 60 Myr after the onset of lithospheric stretching, preserving <300 m after 100 Myr when the surface processes of erosion are neglected (Group I). In scenarios with high crust-mantle coupling (Fig. 6c-e) the escarpment can preserve >1 km related to rifting ($\Delta h_{rift} > 1$ km) after 130 Myr since the onset of rifting when surface processes are neglected. In scenarios of Group I (without erosion), $\Delta h_{post} = 0$ and the escarpment retreat is null ($x_r = 0$).

The post-rift component Δh_{post} is mainly due to the combined effect of erosion of the escarpment and the isostatic and flexural response of the plate to the unloading of the margin [Gilchrist and Summerfield, 1990; Kooi and Beaumont, 1994]. The local unloading of the margin due to erosion of the coastal escarpment is regionally compensated by isostatic flexural rebound, contributing to amplify the elevation of the escarpment. This component also takes into account the effect of the thermal cooling and the lateral flow of the lower crust after rifting. If the preexistent topography is represented by a plateau (h_0= constant), as in scenarios of Group III where we assumed a plateau 1 km above the sea level, the coastal escarpment retreats landward and erodes nearly the same column of rock, inducing the same amount of flexural rebound of the lithosphere, preserving the altitude of the escarpment nearly constant through time.

In scenarios of Group III (Fig. 8 and 9), the altitude of the escarpment for $t > 40$ Myr is nearly 500 m above the initial altitude ($\Delta h_{post} \approx 500$
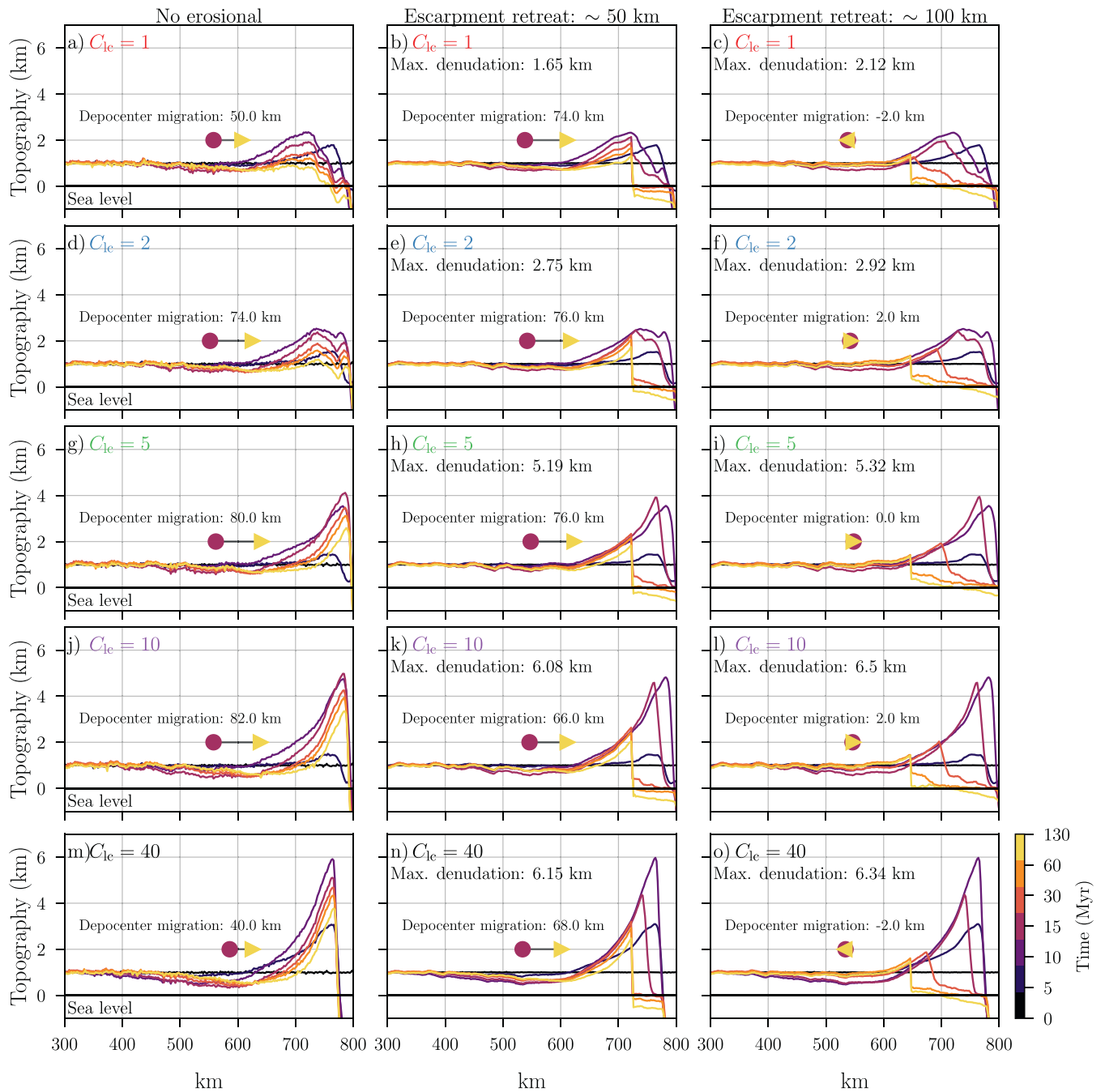
Fig. 8. Topographic evolution for scenarios of groups I-a (1st column), II (2nd column) and III (3rd column). Each row represents the adopted $C_{lc} = 1$ (a-c), 2 (d-f), 5 (g-i), 10 (j-l) and 40 (m-o), respectively. Black horizontal lines represent the sea level. Full circles and triangles represent the position of the depocenter of the flexural basin formed behind the rift flank at 15 and 130 Myr, respectively.

m). In these cases, the total escarpment retreat is $x_r > 100$ km, and consequently the contribution of the rifting on the amplitude of the retreated escarpment is negligible ($\Delta h_{rift} \rightarrow 0$). Only in scenarios where the total escarpment retreat is $x_r \lesssim 100$ km does the rifting have an important contribution to the escarpment amplitude, like in scenarios of Group II, where the retreat was nearly 50 km.

4.3. Comparison with natural margins

To compare the natural escarpments with the numerical results presented here, we removed the regional component of the topography of the continental margins. This procedure is described in the Supplementary Material. This regional component is related to the long-

wavelength features of the preexistent topography h_0 and/or dynamic topography that vertically displace a large extent of the continent. Therefore, the removal of the regional component aims to isolate the uplift of the margin related to rifting and post-rift processes associated with the interaction of flexure and surface processes. One limitation of this procedure is that short-wavelength features related to the pre-rift topography h_0 cannot be removed and can affect the amplitude of the calculated residual topography of the escarpment.

The mean regional elevation ($\bar{h}_{mean}$) for each escarpment (Fig. 1) was obtained calculating the mean elevation of the interior of the continent without the contribution of the coastal escarpment (see Supplementary Materials S2). Subtracting $\bar{h}_{mean}$ from the mean present-day elevation of
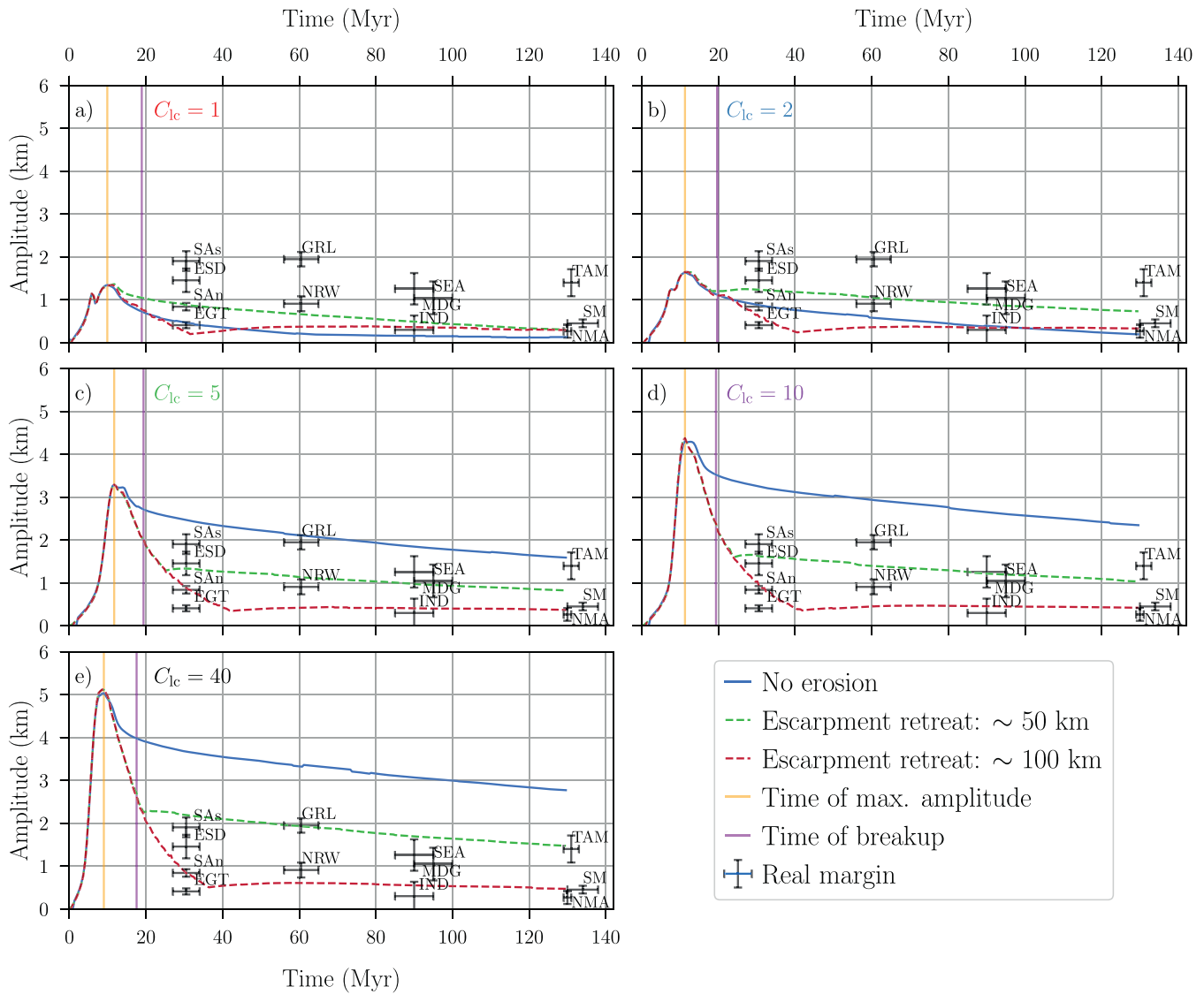
Fig. 9. (a-e) Evolution of the escarpment amplitude (elevation difference between maximum escarpment elevation and the plateau) of the left margin. Scenarios with no erosion (blue lines), high erosion (dashed red lines) and mild erosion (dashed green lines), for $C_{lc} = 1$ (a), 2 (b), 5 (c), 10 (d) and 40 (e), respectively. Light orange and light purple vertical lines indicates the instant of maximum amplitude of rift flank and the time of break up, respectively. Error bars represent the mean amplitude of escarpments of residual topography ($\overline{h}_{res}$) of the natural margins according to margin age as presented in Supplementary Table 1. SM: Serra do Mar, NMA: Namibia-Angola; SEA: Southeastern Australia; SAn: Northern Saudi Arabian; EGT: Egypt; ESD: Eritrea-Sudan; SAs: Southern Saudi Arabian; TAM: Trans-antarctic Mountains; IND: India (Western Ghats); MDG: Madagascar; NRW: Norway; GRL: Greenland.

the escarpment gives the mean residual topography $\overline{h}_{res}$ for the coastal escarpment. This residual topography was directly compared with the escarpment amplitude observed in the numerical scenarios (Figs. 6 and 9). This uplift represents the sum $\Delta h_{rift} + \Delta h_{post}$, keeping in mind that $\Delta h_{post} = 0$ for Group I (scenarios without erosion).

In general, the residual topography of the coastal escarpment $\overline{h}_{res}$ tends to decrease with the age of the margin (Fig. 6). Based on our results, part of this decrease of $\overline{h}_{res}$ with margin age can be explained by the viscous relaxation of the lithosphere and thermal cooling of the margin. Additionally, the erosion of the coastal escarpment can decrease its initial amplitude depending on the amount of escarpment retreat (Fig. 9).

The residual topography $\overline{h}_{res}$ is larger than Δh_{rift} for the scenario with $C_{lc} = 1$ (Fig. 6a), except for the mature margins of South Atlantic (Serra do Mar escarpment in Brazil and escarpments along the Namibia and Angola margins), where this scenario with low crust-mantle coupling is

still compatible. The amplitudes of Δh_{rift} obtained in the scenarios with $C_{lc} \geq 10$ (Fig. 6d-e) are non-realistic compared with the amplitude observed along divergent margins of different ages. These scenarios can only be compatible with the observed margins if the erosional exhumation of the margin is larger than 5–6 km and escarpment retreat is larger than 50 km (Figs. 8d,e,i,j and 9d-e).

On the other hand, scenarios with intermediate crust-mantle coupling ($C_{lc} = 2$-5) are compatible with the majority of the escarpments in margins with different ages (Fig. 6b-c). In these scenarios, the amplitude of the escarpment uplift differs 500–800 m between the conjugated margins, creating an asymmetry between the margins compatible with the the difference in $\overline{h}_{res}$ in some conjugated margins (Red Sea escarpments and Greenland-Norway escarpments, Fig. 6).

When the escarpment retreat due to erosion is taken into account, the magnitude of the retreat will control the rifting influence on the preservation of the escarpment in mature margins. As observed in our numerical experiments, if the retreat is larger than 100 km, the amplitude

of the escarpment will have negligible influence from the inherited topographic effects of rifting. This is probably the case for the Serra do Mar escarpments in southeastern Brazil, where the total retreat is of the order of 100–150 km, assuming that the initial escarpment was formed along the Cretaceous ringe line [Karner and Gambôa, 2007]. Therefore, we suggest that the present-day escarpments in southeasthern Brazil have inexpressive contribution from rifting on its current amplitude ($\Delta h_{rift} \rightarrow 0$). In this case, the preexistent topography h_0 (before the onset of lithospheric stretching) combined with the Paraná Magmatic Province that preceded the rifting can contribute to create an initial elevation >1 km high. Additionally, post-rift tectonism that formed the Continental Rift of Southeastern Brazil [Riccomini, 1989] possibly contributed to amplify the present elevation of the escarpment.

Similarly, the escarpments in southern Africa probably retreated >100 km [van der Beek et al., 2002], and therefore the current amplitude of the escarpment has almost no relation to the amplitude of the rift flank uplift. The high amplitude of the escarpment sustained along the margins in southern Africa is probably related to post-rift processes, created by continental scale uplift induced by mantle dynamics [Braun et al., 2014].

In contrast, the mature margin in southeastern Australia has a total escarpment retreat of only a few tens of kilometers resulting in an offshore margin with narrow sedimentary package [Sacek et al., 2012; Shaw, 1990]. In this case, we propose that the rifting flank uplift is an important component preserving the present altitude of the southeastern Australian escarpment. In fact, the amplitude of the present escarpment in southeastern Australia is compatible with our models with intermediate degree of crust-mantle coupling ($C_{lc} = 5$) with escarpment retreat smaller than 50 km (see SEA in Fig. 9c).

Relatively young margins around the Red Sea are mainly preserved as a consequence of the uplift induced during rifting and thermal effects due to lithospheric thinning, probably contributing with 1–2 km of the amplitude of the current escarpment. In combination with these processes, upper mantle thermal anomalies can also amplify the regional uplift of the margin [Daradich et al., 2003], especially in the Arabian Plate. Our scenarios with low degree of crust-mantle coupling ($C_{lc} = 2$, Fig. 6b) obtained amplitude of escarpments compatible with the ones observed along the conjugate margins of the Red Sea.

The comparison of the present numerical results with different natural escarpments around the world suggests that the degree of crust/
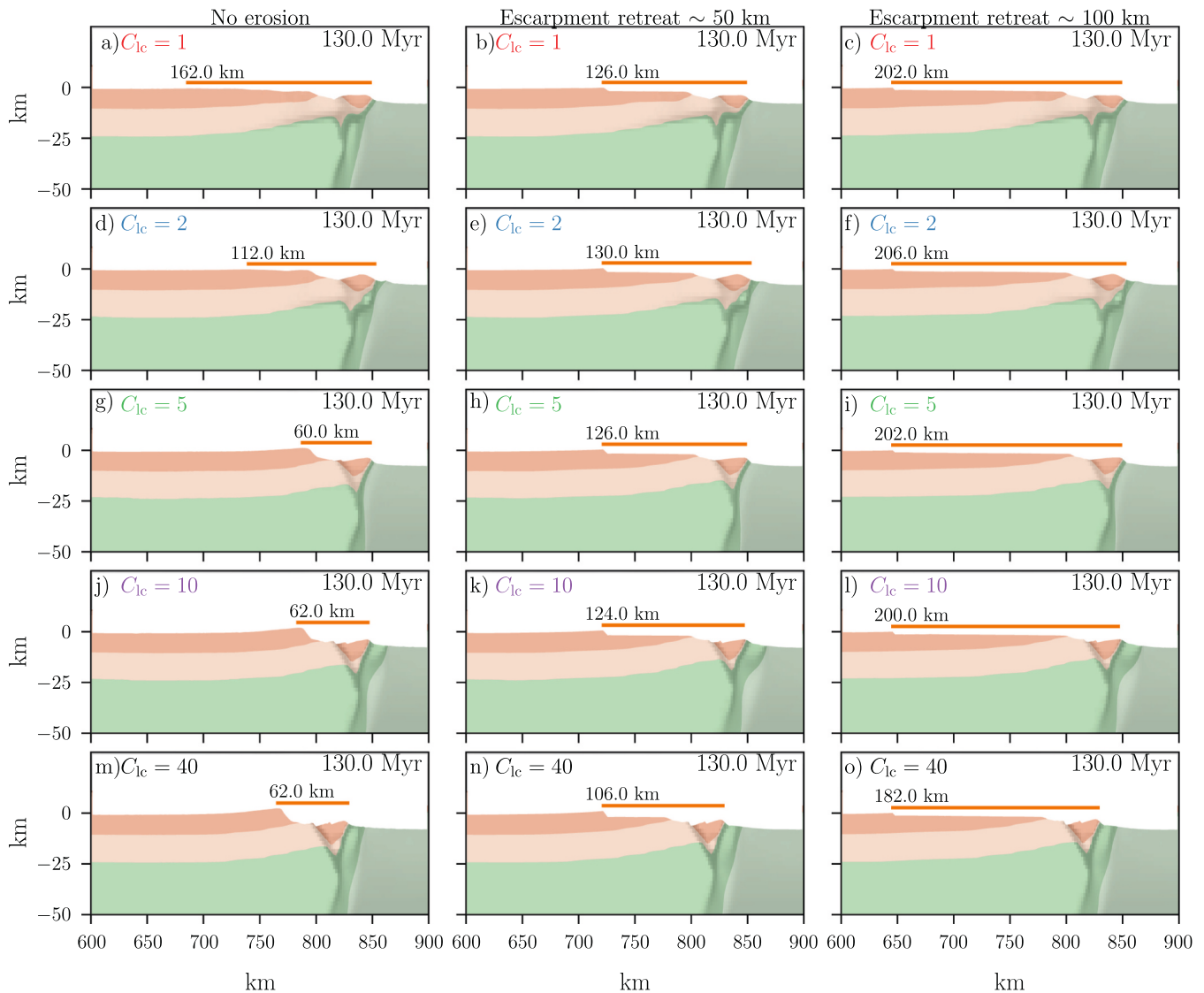
Fig. 10. Final left margin geometry for scenarios of groups I-a (1st column), II (2nd column) and III (3rd column). Each row shows models with $C_{lc} = 1$ (a-c), 2 (d-f), 5 (g-i), 10 (j-l) and 40 (m-o), respectively. Shaded areas represents the cumulative strain. Dark and light orange represents upper and lower crust, respectively. Dark and light green represents lithospheric mantle and asthenosphere, respectively. Orange bars indicates the width of apparent taper length (ATL). (For interpretation of the references to colour in this figure legend, the reader is referred to the web version of this article.)

lithospheric mantle coupling along continental margins can be classified as weak to intermediate, with $C_{lc} < 10$. In our simplified analysis, we explored only the re-scaling of the viscosity factor for the lower crust C_{lc}, assuming that initially the thermal state of the lithosphere is close to conductive equilibrium and the lithosphere is horizontally homogeneous. However, thermal perturbations prior to the rifting phase [Buck, 2007] and the presence of fluids [e.g. Chen et al., 2006] can significantly weaken the lithosphere, decreasing the lithospheric coupling in the rifting zone [Burov, 2011]. Therefore, we propose that part of the decoupling observed along these margins can be explained by thermal effects and/or due to metasomatic processes.

4.4. Apparent taper length and escarpment amplitude

Osmundsen and Redfield [2011] correlated the amplitude of several escarpments worldwide with the apparent taper length (ATL), which is defined as the distance from the top of coastal escarpment to the first location oceanward where the crustal thickness reaches 10 km or less (taper break). They found an inverse correlation between the ATL and escarpment amplitude: Escarpments with low amplitudes had a smooth gradient of crustal thinning and a larger ATL whereas escarpments with higher amplitudes had a sharp transition from normal to thinned crust.

To compare the observed ATL for different margins with our numerical results, we calculated the equivalent ATL as the distance from the top of escarpment (rift flank) to the first location oceanward where crustal thickness reaches 5 km or less (Fig. 10). This criterion was used to
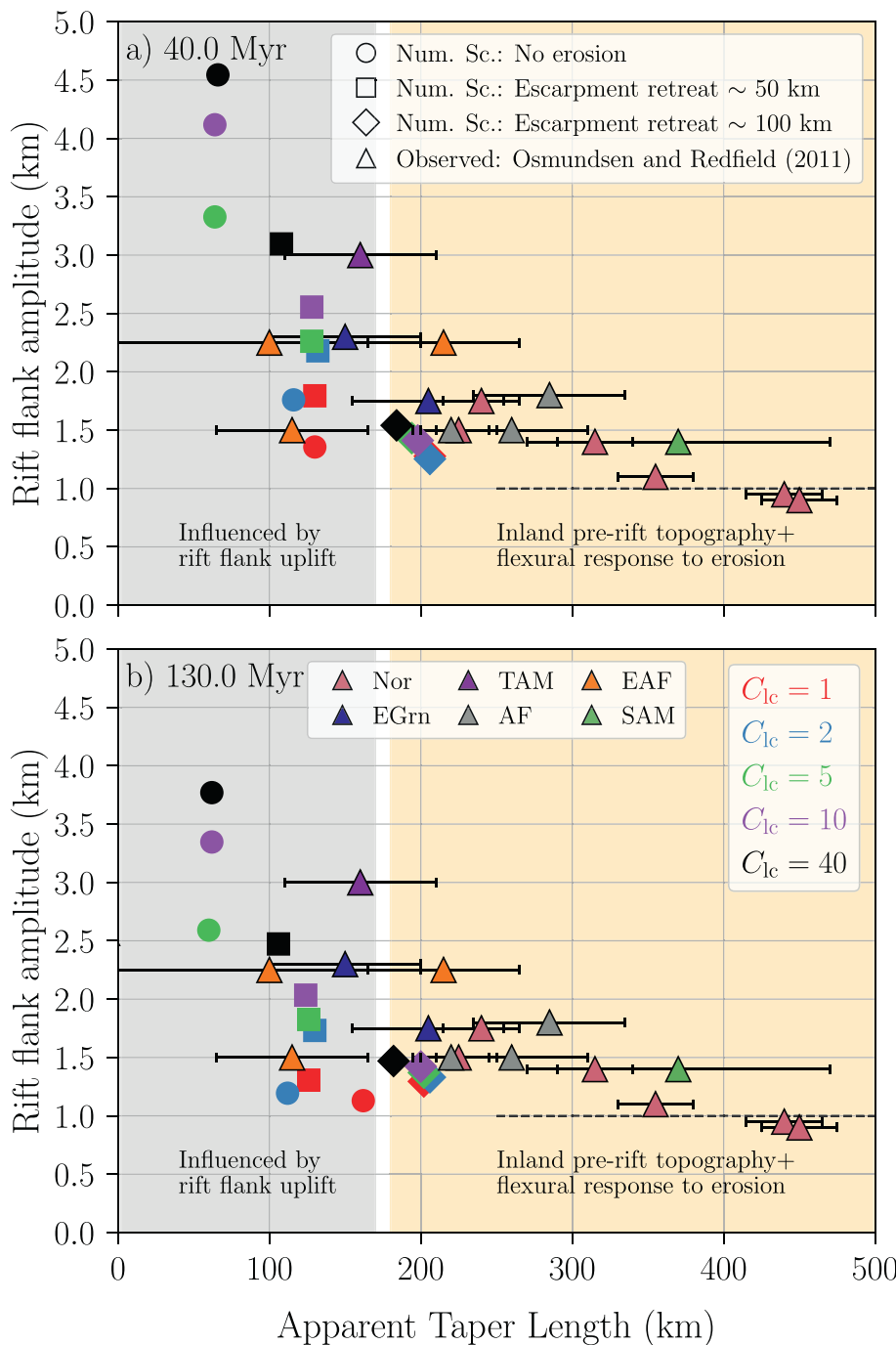
Fig. 11. Rift flank amplitude as a function of apparent taper length (ATL) for groups I-a (circles), II (squares) and III (diamonds) at 40 (a) and 130 Myr (b). The symbol colour represent C_{lc}. red: $C_{lc} = 1$; blue: $C_{lc} = 2$; green: $C_{lc} = 5$; purple: $C_{lc} = 10$; black: $C_{lc} = 40$. Triangles with error bars represents the data-set presented by Osmundsen and Redfield [2011]. Black dashed line represents the lower limit for rift flank for erosional scenarios. Nor (rose): Norway, EGrn (royal blue): East Greenland, TAM (bright purple): Transantarctic Mountains, AF (gray): Africa (Namibia), EAF (orange): East Africa (red sea), SAM (fern green): South Atlantic Margin. (For interpretation of the references to colour in this figure legend, the reader is referred to the web version of this article.)

keep the coherence of the measured ATL through time in the numerical simulations because the rotation of crustal blocks during *syn-* and post-rift phase changed the measured value of ATL defined by Osmundsen and Redfield [2011] (crustal thickness ≤ 10 km).

In the scenarios with no erosion at 130 Myr after the onset of the lithospheric stretching (Group I-a, Fig. 10, first column), there is an inverse correlation between the ATL and escarpment amplitude: for example, the scenario with $C_{lc} = 1$ resulted in ATL = 162 km with escarpment amplitude of 1.2 km, while the scenario with $C_{lc} = 10$ obtained 62 km of ATL and escarpment amplitude of 3.4 km.

However, when we consider the effects of surface processes, variations in the ATL are essentially controlled by the magnitude of escarpment retreat of the margin, which is guided by surface processes and is not directly related to the rifting style. In our scenarios with imposed escarpment retreat due to erosion, the ATL was between 106 and 130 km for Group II and 182–206 km for Group III, without a clear correlation with the rifting style (Fig. 10, second and third columns).

The correlation between the ATL and escarpment amplitude derived from the numerical scenarios present a similar pattern of the global compilation obtained by Osmundsen and Redfield [2011] (Fig. 11). Due to viscous relaxation and thermal dissipation, the amplitude of escarpments decrease through time (compare the numerical scenarios at 40 Myr, Fig. 11a, and 130 Myr, Fig. 11b). Therefore the correlation between ATL and escarpment amplitude can vary through time even in a scenario without surface processes. For the scenarios with escarpment retreat (Groups II and III, squares and diamonds in Fig. 11) the decrease in escarpment amplitude and consequent increase in ATL relative to the scenarios without erosion (circles in Fig. 11) occurred only due to surface processes, and is not related to the rifting process. For scenarios with larger escarpment retreat, >100 km, we expect that the amplitude of the escarpment will reach the minimum amplitude of the initial 1 km plateau (indicated as the dashed line in Fig. 11), or values just above this minimum due to flexural response to the erosion of the coastal region. In this case, the amplitude of the escarpment is related solely to the pre-rift topography of the interior of the continent, without the influence from the rifting style.

In fact, the definition of the ATL combines two independent components: (1) the width of the stretched margin and (2) the magnitude of the escarpment retreat. Based on the flexural wavelength observed in the numerical simulations, we propose here that only for relatively narrow ATL (<150 − 200 km) the inverse correlation between escarpment amplitude and ATL is due to the rifting style and the flexural response of the margin due to lithospheric stretching (gray region in Fig. 11). On the other hand, for ATL larger than 150–200 km, the amplitude of the escarpment is probably related to pre-rift elevation of the interior of the margin (orange region in Fig. 11).

4.5. Model limitations

Other geodynamic processes can affect the amplitude of Δh_{rift}, like edge-driven convection and magmatic underplating. Edge-driven convection [King and Anderson, 1998] induced by the lateral variation in lithospheric thickness can also dynamically perturb the continental margin, but this is a secondary effect unless the convection induces erosion of the border of the continental lithospheric mantle [e.g. Sacek, 2017], which is a process not explored in the present work. Magmatic underplating, which was not considered in our numerical simulations, can induce crustal uplift with amplitude of 10–16% of the underplating thickness, assuming simple isostatic equilibrium [Watts, 2001].

As previously discussed, in this work we tested only the effects of the amount of escarpment retreat on the preservation of rift flank topography in the long-term evolution of the margin assuming a simplified surface processes model. However, the incorporation of more realistic surface processes model fully coupled with the thermo-mechanical model [e.g. Beucher and Huismans, 2020; Theunissen and Huismans, 2019], is fundamental to analyse the feedback mechanisms of the interaction between surface and internal processes.

Vertical displacements of the continent due to large scale mantle convection cells (dynamic topography) with wavelength larger than 1000 km certainly can affect the amplitude of coastal escarpment along the margin, representing one additional component for Δh_{post} not considered here. However, this long-wavelength component affects a large portion of the continent and can be filtered in our analysis, as discussed in section 4.3.

In our experiments, the surface processes do not considered the sedimentation along the offshore margin. Additionally, the load of the sedimentary layer can amplify the subsidence of the onshore margin due to flexural effects, specially in portions close to the hinge zone. Therefore, we expect that the amplitude of the coastal escarpment predicted in our work represents a upper limit, and the load along the stretched margin due to sedimentation can amplify the subsidence of the margin during the post-rift phase of the margin, especially in scenarios where the escarpment retreat was <50 km.

5. Conclusions

The use of 2D thermo-mechanical numerical simulations and the comparison of the results with natural escarpments along rifted margins allowed us to obtain the following conclusions about the influence of the rheological structure of the lithosphere and magnitude of escarpment retreat on the preservation of escarpments through the geological evolution of the margin:

- The amplitude of the coastal escarpment is a function of the degree of coupling between the crust and lithospheric mantle. In the numerical scenarios, strong crust allows the development of high rift flank elevation. However, the maximum amplitude of the coastal escarpment is less sensitive to stretching rate of the lithosphere.
- The flexural wavelength of the rift flank uplift created during lithospheric stretching is limited to 100–150 km, independent of the rheological structure of the lower crust.
- The maximum escarpment amplitude formed during the lithospheric stretching decreases monotonically during the post-rift phase due to ductile flow of the lower crust and thermal cooling of the margin.
- The depocenter of the negative forebulge in the interior of the continent developed concomitantly with the rift flank uplift, with amplitude of few hundreds of meters, and migrates a few tens of kilometers towards the coastal escarpment in scenarios with limited escarpment retreat (≤50 km). This migration is limited or nonexistent in scenarios with large escarpment retreat, of the order of 100 km.
- When the extent of escarpment retreat due to erosion is larger than 100 km, the resulting escarpment is mainly sustained by the feedback mechanism between erosional unloading and isostatic response of the lithosphere and/or post-rift regional uplift. This is probably the case for the escarpments of the conjugate margins of the South Atlantic Ocean.
- The coastal escarpment in Southeastern Australia can probably preserve a large fraction of the influence of the rift flank uplift due to the relatively small amount of escarpment retreat since the onset of rifting.

Supplementary data to this article can be found online at https://doi.org/10.1016/j.tecto.2023.229769.

CRediT authorship contribution statement

João Pedro Macedo Silva: Validation, Formal analysis, Investigation, Writing – original draft, Data curation, Visualization. **Victor Sacek:** Conceptualization, Methodology, Software, Resources, Writing – review & editing, Supervision. **Rafael Monteiro da Silva:** Software, Writing – review & editing.

Declaration of Competing Interest

The authors declare that they have no known competing financial interests or personal relationships that could have appeared to influence the work reported in this paper.

Data availability

Data will be made available on request.

Acknowledgements

References

Amante, Christopher, Eakins, Barry W., 2009. Etopo1 arc-minute global relief model: procedures, data sources and analysis. In: NOAA Technical Memorandum NESDIS NGDC-24. URL. https://repository.library.noaa.gov/view/noaa/1163/noaa_1163_DS1.pdf.

An, Meijian, Assumpção, Marcelo, 2006. Crustal and upper mantle structure in the intracratonic Paraná Basin, SE Brazil, from surface wave dispersion using genetic algorithms. J. S. Am. Earth Sci. 21 (3), 173–184. https://doi.org/10.1016/j.jsames.2006.03.001.

Andrés-Martínez, Miguel, Pérez-Gussinyé, Marta, Armitage, John, Morgan, Jason P., 2019. Thermomechanical implications of sediment transport for the architecture and evolution of continental rifts and margins. Tectonics 38 (2), 641–665. https://doi.org/10.1029/2018TC005346.

Beaumont, Christopher, Keen, Charlotte E., Boutilier, Ross, 1982. On the evolution of rifted continental margins: comparison of models and observations for the nova scotian margin. Geophys. J. Int. 70 (3), 667–715.

van der Beek, Peter, Andriessen, Paul, Cloetingh, Sierd, 1995. Morphotectonic evolution of rifted continental margins: Inferences from a coupled tectonic-surface processes model and fission track thermochronology. Tectonics 14 (2), 406–421. https://doi.org/10.1029/94TC02445.

van der Beek, Peter, Summerfield, Michael A., Braun, Jean, Brown, Roderick W., Fleming, Alastair, 2002. Modeling postbreakup landscape development and denudational history across the southeast African (Drakensberg Escarpment) margin. J. Geophys. Res. Solid Earth 107 (B12). https://doi.org/10.1029/2001JB000744. ETG–11.

Beucher, Romain, Huismans, R.S., 2020. Morphotectonic evolution of passive margins undergoing active surface processes: Large-scale experiments using numerical models. Geochem. Geophys. Geosyst. 21 (5), e2019GC008884 https://doi.org/10.1029/2019GC008884.

Bradley, Dwight C., 2008. Passive margins through earth history. Earth Sci. Rev. 91 (1–4), 1–26. https://doi.org/10.1016/j.earscirev.2008.05.001.

Braun, Jean, 2010. The many surface expressions of mantle dynamics. Nat. Geosci. 3 (12), 825–833. https://doi.org/10.1038/ngeo1020. ISSN 17520908.

Braun, Jean, 2018. A review of numerical modeling studies of passive margin escarpments leading to a new analytical expression for the rate of escarpment migration velocity. Gondwana Res. 53, 209–224. https://doi.org/10.1016/j.gr.2017.04.012.

Braun, Jean, Beaumont, Christopher, 1989. A physical explanation of the relation between flank uplifts and the breakup unconformity at rifted continental margins. Geology 17 (8), 760–764. https://doi.org/10.1130/0091-7613(1989)017\%3C0760:APEOTR\%3E2.3.CO;2.

Braun, Jean, Van der Beek, Peter, Batt, Geoffrey, 2006. Quantitative Thermochronology: Numerical Methods for the Interpretation of Thermochronological Data. Cambridge University Press.

Braun, Jean, Guillocheau, François, Robin, Cécile, Baby, Guillaume, Jelsma, Hielke, 2014. Rapid erosion of the Southern African Plateau as it climbs over a mantle superswell. J. Geophys. Res. Solid Earth 119 (7), 6093–6112. https://doi.org/10.1002/2014JB010998.

Brown, Roderick W., Summerfield, Michael A., Gleadow, Andrew J.W., 2002. Denudational history along a transect across the drakensberg escarpment of southern africa derived from apatite fission track thermochronology. J. Geophys. Res. Solid Earth 107 (B12). ETG–10.

Buck, W.R., 2007. Dynamic processes in extensional and compressional settings: The dynamics of continental breakup and extension. In: *Treatise on Geophysics*, Volume Crust and Lithosphere Dynamics, vol. 6. Elsevier, pp. 335–376. https://doi.org/10.1016/B978-044452748-6.00110-3.

Buiter, Susanne, 2021. A discussion on how, when and where surface processes interplay with extensional tectonic deformation. In: EGU General Assembly Conference

Abstracts pages EGU21–8665. URL. https://ui.adsabs.harvard.edu/abs/2021EGUGA..23.8665B/abstract.

Burov, Evgene B., 2011. Rheology and strength of the lithosphere. Mar. Pet. Geol. 28 (8), 1402–1443.

Burov, E., Cloetingh, S.A.P.L., 1997. Erosion and rift dynamics: new thermomechanical aspects of post-rift evolution of extensional basins. Earth Planet. Sci. Lett. 150 (1–2), 7–26. https://doi.org/10.1016/S0012-821X(97)00069-1.

Burov, E., Poliakov, A., 2001. Erosion and rheology controls on synrift and postrift evolution: Verifying old and new ideas using a fully coupled numerical model. J. Geophys. Res. Solid Earth 106 (B8), 16461–16481. https://doi.org/10.1029/2001JB000433.

Chen, S., Hiraga, T., Kohlstedt, David L., 2006. Water weakening of clinopyroxene in the dislocation creep regime. J. Geophys. Res. Solid Earth 111 (B8).

Chery, Jean, Lucazeau, Francis, Daignieres, Marc, Vilotte, Jean-Pierre, 1992. Large uplift of rift flanks: a genetic link with lithospheric rigidity? Earth Planet. Sci. Lett. 112 (1–4), 195–211. https://doi.org/10.1016/0012-821X(92)90016-O.

Crameri, F., Schmeling, H., Golabek, G.J., Duretz, T., Orendt, R., Buiter, S.J.H., May, D. A., Kaus, B.J.P., Gerya, T.V., Tackley, P.J., 2012. A comparison of numerical surface topography calculations in geodynamic modelling: an evaluation of the 'sticky air' method. Geophys. J. Int. 189 (1), 38–54. https://doi.org/10.1111/j.1365-246X.2012.05388.x.

Daradich, Amy, Mitrovica, Jerry X., Pysklywec, Russell N., Willett, Sean D., Forte, Alessandro M., 2003. Mantle flow, dynamic topography, and rift-flank uplift of arabia. Geology 31 (10), 901–904. https://doi.org/10.1130/G19661.1.

Gilchrist, A.R., Summerfield, M.A., 1990. Differential denudation and flexural isostasy in formation of rifted-margin upwarps. Nature 346 (6286), 739–742 (https://www.nature.com/articles/346739a0.pdf).

Gilchrist, Alan R., Kooi, Henk, Beaumont, Christopher, 1994. Post-gondwana geomorphic evolution of southwestern africa: Implications for the controls on landscape development from observations and numerical experiments. J. Geophys. Res. Solid Earth 99 (B6), 12211–12228. https://doi.org/10.1029/94JB00046.

Gleason, Gayle C., Tullis, Jan, 1995. A flow law for dislocation creep of quartz aggregates determined with the molten salt cell. Tectonophysics 247 (1–4), 1–23. https://doi.org/10.1016/0040-1951(95)00011-b.

Gunnell, Y., 2000. Apatite fission track thermochronology: an overview of its potential and limitations in geomorphology. Basin Res. 12 (2), 115–132.

Huismans, Ritske S., Beaumont, Christopher, 2003. Symmetric and asymmetric lithospheric extension: Relative effects of frictional-plastic and viscous strain softening. J. Geophys. Res. Solid Earth 108 (B10), 1–22. https://doi.org/10.1029/2002jb002026. ISSN 2169-9356.

Huismans, Ritske S., Beaumont, C., 2007. Roles of lithospheric strain softening and heterogeneity in determining the geometry of rifts and continental margins. Geol. Soc. Spec. Publ. 282 (0), 111–138. https://doi.org/10.1144/SP282.6. ISSN 03058719.

Huismans, Ritske S., Beaumont, Christopher, 2014. Rifted continental margins: the case for depth-dependent extension. Earth Planet. Sci. Lett. 407 (0), 148–162. https://doi.org/10.1016/j.epsl.2014.09.032.

Jiao, Ruohong, Braun, Jean, Kravitz, Katherine, 2020. Isostatic control of axial rivers and large drainage basins on passive margins. Geophys. Res. Lett. 47 (17), e2020GL089627.

Karato, Shun-ichiro, 1993. Rheology of the upper mantle: A synthesis. Science 260 (5109), 771–778. https://doi.org/10.1126/science.260.5109.771.

Karner, G.D., Gambôa, L.A.P., 2007. Timing and origin of the South Atlantic pre-salt sag basins and their capping evaporites. Geol. Soc. Lond., Spec. Publ. 285 (1), 15–35.

King, Scott D., Anderson, Don L., 1998. Edge-driven convection. Earth Planet. Sci. Lett. 160 (3–4), 289–296. https://doi.org/10.1016/S0012-821X(98)00089-2. ISSN 0012821X.

Kooi, Henk, Beaumont, Christopher, 1994. Escarpment evolution on high-elevation rifted margins: Insights derived from a surface processes model that combines diffusion, advection, and reaction. J. Geophys. Res. Solid Earth 99 (B6), 12191–12209. https://doi.org/10.1029/94JB00047.

McKenzie, Dan, 1984. A possible mechanism for epeirogenic uplift. Nature 307 (5952), 616–618.

Moresi, Louis, Solomatov, Viatcheslav, 1998. Mantle convection with a brittle lithosphere: thoughts on the global tectonic styles of the Earth and Venus. Geophys. J. Int. 133 (3), 669–682, 06 1998. ISSN 0956-540X. https://doi.org/10.1046/j.1365-246X.1998.00521.x.

Nyblade, Andrew A., Sleep, Norman H., 2003. Long lasting epeirogenic uplift from mantle plumes and the origin of the Southern African Plateau. Geochem. Geophys. Geosyst. 4 (12) https://doi.org/10.1029/2003GC000573.

Osmundsen, Per Terje, Redfield, T.F., 2011. Crustal taper and topography at passive continental margins. Terra Nova 23 (6), 349–361. https://doi.org/10.1111/j.1365-3121.2011.01014.x.

Riccomini, Claudio, 1989. O rift continental do sudeste do Brasil. PhD thesis,. Universidade de São Paulo.

Ryberg, Trond, Haberland, Christian, Haberlau, Thomas, Weber, Michael H., Bauer, Klaus, Behrmann, Jan H., Jokat, Wilfried, 2015. Crustal structure of Northwest Namibia: evidence for plume-rift-continent interaction. Geology 43 (8), 739–742. https://doi.org/10.1130/G36768.1.

Sacek, Victor, 2017. Post-rift influence of small-scale convection on the landscape evolution at divergent continental margins. Earth Planet. Sci. Lett. 459 (0), 48–57. https://doi.org/10.1016/j.epsl.2016.11.026. ISSN 0012821X.

Sacek, Victor, Braun, Jean, Van Der Beek, P., 2012. The influence of rifting on escarpment migration on high elevation passive continental margins. J. Geophys. Res. Solid Earth 117 (B4). https://doi.org/10.1029/2011JB008547.

Salazar-Mora, Claudio A., Huismans, Ritske S., Fossen, Haakon, Egydio-Silva, Marcos, 2018. The Wilson cycle and effects of tectonic structural inheritance on rifted passive margin formation. Tectonics 37 (9), 3085–3101. https://doi.org/10.1029/2018TC004962.

Shaw, R.D., 1990. Development of the Tasman Sea and easternmost australian continental margin: a review. Bulletin-Australia, Bureau Mineral Res. Geol. Geophys. 232 (232), 53–66.

Silva, R.M., Sacek, V., 2022. Influence of surface processes on postrift faulting during divergent margins evolution. Tectonics 41. https://doi.org/10.1029/2021TC006808. e2021TC006808.

Sordi, Michael Vinicius, Salgado, André Augusto Rodrigues, Siame, Lionel, Bourlès, Didier, Paisani, Julio Cesar, Léanni, Laëtitia, Braucher, Régis, Do Couto, Edivando Vtor, ASTER Team, et al., 2018. Implications of drainage rearrangement for passive margin escarpment evolution in southern brazil. Geomorphology 306 (0), 155–169. https://doi.org/10.1016/j.geomorph.2018.01.007.

Theunissen, Thomas, Huismans, Ritske S., 2019. Long-term coupling and feedback between tectonics and surface processes during non-volcanic rifted margin formation. J. Geophys. Res. Solid Earth 124 (11), 12323–12347. https://doi.org/10.1029/2018JB017235.

Theunissen, Thomas, Huismans, Ritske S., Gang, Lu, Riel, Nicolas, 2022. Relative continent/mid-ocean ridge elevation: a reference case for isostasy in geodynamics. Earth Sci. Rev. 104153.

Thybo, H., Artemieva, I.M., 2013. Moho and magmatic underplating in continental lithosphere. Tectonophysics 609 (0), 605–619. https://doi.org/10.1016/j.tecto.2013.05.032.

Turcotte, Donald L., Emerman, Steven H., 1983. Mechanisms of active and passive rifting. In: Developments in Geotectonics, 19. Elsevier, pp. 39–50.

Watts, A.B., 2001. Isostasy and Flexure of the Lithosphere. Cambridge University Press.

Weissel, Jeffrey K., Karner, Garry D., 1989. Flexural uplift of rift flanks due to mechanical unloading of the lithosphere during extension. J. Geophys. Res. Solid Earth 94 (B10), 13919–13950.

White, Robert, McKenzie, Dan, 1989. Magmatism at rift zones: the generation of volcanic continental margins and flood basalts. J. Geophys. Res. Solid Earth 94 (B6), 7685–7729.

Widdowson, M., Cox, K.G., 1996. Uplift and erosional history of the Deccan Traps, India: evidence from laterites and drainage patterns of the western ghats and konkan coast. Earth Planet. Sci. Lett. 137 (1–4), 57–69. https://doi.org/10.1016/0012-821X(95)00211-T.

Wojciechowski, Marek, 2018. A note on the differences between drucker-prager and mohr-coulomb shear strength criteria. Studia Geotechnica et Mechanica 40 (3), 163–169. https://doi.org/10.2478/sgem-2018-0016.

Wolf, Lorenz, Huismans, Ritske S., Rouby, Delphine, Gawthorpe, Robert L., Wolf, Sebastian G., 2022. Links between faulting, topography, and sediment production during continental rifting: Insights from coupled surface process, thermo-mechanical modelling. J. Geophys. Res. Solid Earth. https://doi.org/10.1029/2021JB023490 page e2021JB023490.

Zhong, Shijie, Yuen, David A., Moresi, Louis N., Schubert, G., 2007. Numerical methods for mantle convection. Treatise Geophys. 7, 227–252.